Neuroscience, Cell Biology & Physiology Faculty Publications

Neuroscience, Cell Biology & Physiology

3-2-2022

The Anti-Inflammatory Agent Bindarit Attenuates the Impairment of Neural Development through Suppression of Microglial Activation in a Neonatal Hydrocephalus Mouse Model

Eri Iwasawa

Farrah N. Brown

Crystal Shula

Fatima Kahn

Sang Hoon Lee

See next page for additional authors

Authors

Eri Iwasawa, Farrah N. Brown, Crystal Shula, Fatima Kahn, Sang Hoon Lee, Temugin Berta, David R. Ladle, Kenneth Campbell, Francesco T. Mangano, and June Goto

Neurobiology of Disease

The Anti-Inflammatory Agent Bindarit Attenuates the Impairment of Neural Development through Suppression of Microglial Activation in a Neonatal Hydrocephalus Mouse Model

Eri Iwasawa,[1] Farrah N. Brown,[1] Crystal Shula,[1] Fatima Kahn,[1] Sang Hoon Lee,[2] Temugin Berta,[2] David R. Ladle,[3] Kenneth Campbell,[1,4] Francesco T. Mangano,[1,5] and June Goto[1,5]

[1]Division of Pediatric Neurosurgery, Cincinnati Children's Hospital Medical Center, Cincinnati, Ohio, 45242, [2]Pain Research Center, Department of Anesthesiology, University of Cincinnati Medical Center, Cincinnati, Ohio, 45242, [3]Department of Neuroscience, Cell Biology, and Physiology, Wright State University, Dayton, Ohio, 45435, [4]Division of Developmental Biology, Cincinnati Children's Hospital Medical Center, University of Cincinnati College of Medicine, Cincinnati, Ohio, 45242, and [5]Department of Neurosurgery, University of Cincinnati College of Medicine, Cincinnati, Ohio, 45242

Neonatal hydrocephalus presents with various degrees of neuroinflammation and long-term neurologic deficits in surgically treated patients, provoking a need for additional medical treatment. We previously reported elevated neuroinflammation and severe periventricular white matter damage in the *progressive hydrocephalus* (*prh*) mutant which contains a point mutation in the *Ccdc39* gene, causing loss of cilia-mediated unidirectional CSF flow. In this study, we identified cortical neuropil maturation defects such as impaired excitatory synapse maturation and loss of homeostatic microglia, and swimming locomotor defects in early postnatal *prh* mutant mice. Strikingly, systemic application of the anti-inflammatory small molecule bindarit significantly supports healthy postnatal cerebral cortical development in the *prh* mutant. While bindarit only mildly reduced the ventricular volume, it significantly improved the edematous appearance and myelination of the corpus callosum. Moreover, the treatment attenuated thinning in cortical Layers II–IV, excitatory synapse formation, and interneuron morphogenesis, by supporting the ramified-shaped homeostatic microglia from excessive cell death. Also, the therapeutic effect led to the alleviation of a spastic locomotor phenotype of the mutant. We found that microglia, but not peripheral monocytes, contribute to amoeboid-shaped activated myeloid cells in *prh* mutants' corpus callosum and the proinflammatory cytokines expression. Bindarit blocks nuclear factor (NF)-kB activation and its downstream proinflammatory cytokines, including monocyte chemoattractant protein-1, in the *prh* mutant. Collectively, we revealed that amelioration of neuroinflammation is crucial for white matter and neuronal maturation in neonatal hydrocephalus. Future studies of bindarit treatment combined with CSF diversion surgery may provide long-term benefits supporting neuronal development in neonatal hydrocephalus.

Key words: bindarit; microglia; neonatal hydrocephalus; white matter injury

Significance Statement

In neonatal hydrocephalus, little is known about the signaling cascades of neuroinflammation or the impact of such inflammatory insults on neural cell development within the perinatal cerebral cortex. Here, we report that proinflammatory activation of myeloid cells, the majority of which are derived from microglia, impairs periventricular myelination and cortical neuronal maturation using the mouse *prh* genetic model of neonatal hydrocephalus. Administration of bindarit, an anti-inflammatory small molecule that blocks nuclear factor (NF)-kB activation, restored the cortical thinning and synaptic maturation defects in the *prh* mutant brain through suppression of microglial activation. These data indicate the potential therapeutic use of anti-inflammatory reagents targeting neuroinflammation in the treatment of neonatal hydrocephalus.

Introduction

Neonatal hydrocephalus is a life-long incurable condition. Surgical diversion of excess CSF from the cerebral ventricles, via ventriculo-peritoneal shunt placement or endoscopic third ventriculostomy, often requires multiple revisions in young children. Sixty percent of surgically treated patients suffer from neurologic symptoms, including motor skills impairment, cognitive deficits, or epilepsy, throughout life (Pattisapu, 2001; Vinchon et al., 2012; Paulsen et al., 2015). This demonstrates an unmet need to develop early and/or supplemental medical interventions to prevent irreversible pathologic damage in the developing hydrocephalic brain (Robinson, 2012; Del Bigio and Di Curzio, 2016; Karimy et al., 2020a). The impact of hydrocephalus in perinatal human brains is significant as it affects organized neuronal connectivity, synaptogenesis, and myelination, which begins in the third trimester of gestation lasting until early childhood (Kostović and Jovanov-Milošević, 2006; Bercury and Macklin, 2015; Bouyssi-Kobar et al., 2016). In rodents, these cellular processes mostly occur during the early postnatal period (Ross et al., 2015).

Neuroinflammation is commonly described in animal models of hydrocephalus (Wys-Coray et al., 1995; Miller and McAllister, 2007; Deren et al., 2010; Lattke et al., 2012; Goulding et al., 2020; Klebe et al., 2020; Wu et al., 2020), along with pathophysiological and behavioral phenotypes representing neural developmental delays such as hypomyelination (Del Bigio, 2001; Ayannuga et al., 2016), less/shorter branches of the dendrites with less dendritic spines (McAllister et al., 1985; Kriebel et al., 1993), and cognitive deficits (Suda et al., 1994; Jones et al., 1995).

Mononuclear myeloid cell activation has been described in periventricular tissue of fetal brains with hydrocephalus (Ulfig et al., 2004; Dominguez-Pinos et al., 2005) and rodent models (McAllister et al., 1998; Miller and McAllister, 2007; Goulding et al., 2020). Notably, several recent animal studies showed detrimental function of proinflammatory myeloid cells in hydrocephalus progression and tissue damage (McAllister and Miller, 2010; Lattke et al., 2012; Botfield, 2013; Abdi et al., 2018; Wu et al., 2020). However, the detailed definition of these active myeloid cells in pediatric hydrocephalus remains largely unknown (Del Bigio, 2010).

Motile cilia on ependymal cells of the ventricular walls are responsible for generating directional CSF flow within the ventricles. Genetic mutations affecting the development of multiciliated ependymal cells are responsible for a small proportion of congenital hydrocephalus cases (Badano et al., 2006; Feldner et al., 2017; Furey et al., 2018; Lalioti et al., 2019; Wallmeier et al., 2019; Robson et al., 2020). We previously described early and late neuroinflammation phenotypes (Emmert et al., 2019; Goulding et al., 2020) in a robust rodent model of neonatal hydrocephalus, caused by loss of a motile cilia gene, *coiled-coil domain-containing 39* (*Ccdc39*) and the subsequent intraventricular CSF flow retardation contributing to the progressive hydrocephalus (*prh*) phenotype (Abdelhamed et al., 2018). In the *prh* mutant rat, CD68-positive activated myeloid cells start to accumulate in the periventricular tissue at early stages of ventriculomegaly, expressing monocyte chemoattractant protein-1 (MCP-1; Emmert et al., 2019). These myeloid cells also expressed other proinflammatory signals such as CD86 in the corpus callosum of the *prh* mutant mice (Goulding et al., 2020).

Bindarit (2-methyl-2-[[1-(phenylmethyl)-1H-indazol-3-yl] methoxy]-propanoic acid) is a synthetic indazole derivative with an inhibitory effect on the nuclear factor (NF)-kB pathway on various inflammatory stimuli. It attenuates monocyte recruitment (Raghu et al., 2017) and myeloid cell activation (Shen et al., 2021) via reducing IkBα and p65 phosphorylation and the downstream target MCP-1 expression (Mora et al., 2012). Anti-inflammatory effects of bindarit have been demonstrated in various disease models, including arthritis (Rulli et al., 2009), pancreatitis (Bhatia et al., 2005), epilepsy (Cerri et al., 2016), ethanol-induced neuroinflammation (Zhang et al., 2018b), and experimental autoimmune encephalitis (EAE; Ge et al., 2012).

Here, we report the neuroprotective effects of bindarit in a genetic neonatal hydrocephalus model by suppressing proinflammatory microglia. Our findings demonstrate improvement in perinatal brain development and highlight the potential of early intervention to proinflammatory responses as a therapeutic strategy to provide an improved approach for treating neurologic symptoms in neonatal hydrocephalus.

Materials and Methods

Mice and body size measurements
The *Ccdc39^{prh}* allele (i.e., *prh* mice; Stottmann et al., 2011) was maintained on a mixed congenic strain background (50% CD-1 background). Heterozygous *Ccdc39^{wt/prh}* male and female were crossed, and age-matched for both sexes of homozygous *Ccdc39* mutant (*Ccdc39^{prh/prh}*, hereafter *prh*) and wild-type (*Ccdc39*w/w, hereafter WT) mice were used. Mice were housed in specific pathogen-free conditions, and all experiments were performed according to the Institutional Animal Care and Use Committee guidelines of the Cincinnati Children's Hospital Medical Center.

Body weight and head size were measured daily from postnatal day (P)4 through P8. Head size was measured using a caliper as a sum of lengths in three directions of the head; top-bottom (parallel to chin direction), left-right (ear to ear), and rostral (just anterior to zygomatic bone)-caudal (posterior to occipital bone), in millimeter accurate to ±0.01 mm.

Genotyping
DNA was prepared from mouse toes by adding 50 mM NaOH, boiling at 95°C for 30 min, and finally adding Milli-Q water with pH 8 Tris buffer. Genotyping of the *prh* mouse line was done using TaqMan Sample-to-SNP kit (Applied Biosystems) for a single-nucleotide change at chr3: g.33731448A>T (assay ID: AH6R6X7).

Administration of drugs
Bindarit was obtained from Cayman Chemical Company, dissolved at 20 mg/ml in ethanol (for the experiment in Figs. 3, 4A–D) or 100 mg/ml at dimethylsulfoxide (DMSO; Sigma-Aldrich; for the experiment except above), and stored at −20°C for up to three months. DMSO was used over concerns of ethanol-related dermatitis, and the animals with severe dermatitis were removed from the experiment (<10% occurrence). qRT-PCR results showed no difference between the two vehicles in the expression level of *Mcp-1* relative to a housekeeping gene *Gapdh*. On the day of administration, bindarit in ethanol was diluted in 5% Tween 80 (Sigma-Aldrich) and 5% polyethylene glycol 400 (Sigma-Aldrich), and bindarit in DMSO was diluted in 90% corn oil. P4 mouse pups of either sex were randomly assigned to the vehicle or bindarit treatment groups. Bindarit was given at 100 mg/kg body weight subcutaneously daily from P4 through P7. For the vehicle group, either the same amount of ethanol diluted in 5% Tween 80, 5% polyethylene glycol 400, or DMSO diluted in 90% corn oil was injected. The dose of bindarit was determined based on the previous reports (Cerri et al., 2016).

Pharmacokinetic analysis
For pharmacokinetic analysis, bindarit was given once at P7 or four times (P4, P5, P6, P7) subcutaneously to WT or *prh* mutant mouse. Mice were killed at 0, 3, 12, 24, or 48 h after drug administration, blood was collected in lithium heparin tubes, and plasma was isolated by centrifugation at 5000 rpm for 5 min. Brains and livers were then quickly

removed and frozen in liquid nitrogen, and all the samples were sent to Charles River Laboratories, where further measurement was performed. Bindarit levels were determined after solid-phase extraction using liquid chromatography/tandem mass spectrometry (LC/MS/MS) on an API-6500 (Applied Biosystems) instrument. Organ samples were homogenized at $5\times$ in 80:20 in water:acetonitrile. Samples were then diluted at an additional $2\times$ into plasma for a final dilution factor of $10\times$ and run against a plasma curve.

RNA extraction and quantitative RT-PCR
Total RNA treated with DNase was extracted from a sagittal half hemisphere of the cerebrum of P8-P10 mice using RNeasy Plus Mini kit (QIAGEN). cDNA was synthesized using the SuperScript VILO cDNA Synthesis kit (Thermo Fisher Scientific). Quantitative real-time PCR was performed with QuantStudio 5 using PowerUp SYBR Green Master Mix (Thermo Fisher Scientific) according to the manufacturer's instructions, and mRNA expression relative to housekeeping gene *Gapdh* mRNA was calculated with two technical replicates for each biologically independent sample. Primer sequences are listed in Table 1.

nCounter mouse inflammation panel v2
Total RNA from nontreated WT and *prh* samples at P8 ($n = 6$ in each group) extracted above were sent to NanoString. Direct mRNA expression levels of the samples were measured using the NanoString nCounter gene expression system. In all, each 100 ng of total RNA was hybridized with probes from the nCounter Mouse Inflammation v2 panel (NanoString) at 65°C for 16–19 h according to the nCounter Gene Expression Assay Manual. Excess probes were washed away using a two-step magnetic bread-based purification on the nCounter Prep Station (GEN1). The nCounter Digital Analyzer (GEN1) was used to count individual fluorescent barcodes and quantify target molecules present in each sample. For each assay, a high-density scan (600 fields of view) was performed. Gene expression data were analyzed using nSolver analysis software (NanoString) and the Molecular Signatures Database (MSigDB; Subramanian et al., 2005). Pathway scoring using nSolver was performed based on Reactome pathway database gene set (Fabregat et al., 2016), and the gene enrichment analysis (GSEA) using MSigDB was performed on C8: Cell type signature gene sets (http://www.gsea-msigdb.org/gsea/msigdb/).

Immunofluorescence staining, imaging, and quantification
Brains quickly removed from *prh* and WT mice aged embryonic day (E) 18 to P8 ($n = 142$) were fixed in 4% paraformaldehyde (PFA; in PBS) overnight at 4°C. Samples were then washed with PBS, and cryoprotected in 30% sucrose in PBS then immersed in NEG50 freezing medium (Thermo Fisher Scientific); 12-µm-thick cryosections were prepared. For the immunofluorescence staining, sections for nuclear staining (NeuN, SATB2, CTIP2, TBR1, DLX5, and Ki67) were permeabilized with 0.3% Triton X-100 (Thermo Fisher Scientific) in PBS for 30 min. Sections were then incubated with primary antibodies of either anti-mouse glial fibrillary acid protein (GFAP; 1:500, Sigma, G3893), anti-rabbit IBA1 (1:500, Wako, 019-19741), anti-goat IBA1 (1:500, Abcam, ab5076), anti-rabbit OLIG2 (1:500, Abcam, ab136253), anti-rabbit CNPase (1:100, Cell Signaling, 5664), anti-rat CD68 (1:100, Abcam, ab31630), anti-rabbit GLUT1 (1:100, Abcam, ab128033), anti-rabbit neurofilament H (NF-H; 1:500, Millipore AB1989), anti-rat C3AR (1:100, Bioss, BS1101R), anti-rabbit Ki67 (1:200, Abcam, ab15580), anti-mouse SATB2 (1:50, Abcam, ab51502), anti-rat CTIP2 (1:1000, Abcam, ab183032), anti-rabbit TBR1 (1:1000, Abcam, 183032), anti-rabbit neuronal nuclei (NeuN; 1:500, Cell Signaling, D4G40), anti-rabbit DLX5 (generously provided by Prof. John Rubenstein, University of California, San Francisco; Lindtner et al., 2019), anti-rabbit Calbindin D28K (CALB; 1:2000, Millipore, IHCR1013-6), anti-goat Calretinin (CALR; 1:2000, Millipore, AB1550), anti-guinea pig vesicular GABA transporter (VGAT; 1:500, Chemicon, AB5855), and anti-rabbit Gephyrin (GPHN; 1:500, Abcam, ab32206) overnight after the blocking in 0.25% normal donkey serum/0.25% Triton X-100/PBS for 1 h. After stringent washings and subsequent incubation with fluorophore-conjugated secondary antibodies for 2 h, the sections were

counterstained with DAPI (Sigma-Aldrich) for 5 min and mounted with DAPI-Fluoromount-G mounting medium (Southern Biotech). For NF-kB p65 staining, antigen retrieval with citric buffer (pH 6) at 95°C for 45 min, along with tyramide signal amplification was performed. Briefly, sections were treated with 3% H_2O_2 solution for 1 h after the antigen retrieval, and blocking, and anti-rabbit NF-kB p65 (1:100, Cell Signaling, #8242) incubation overnight followed. On the second day, after stringent washings, anti-rabbit IgG biotinylated antibody was incubated for 2 h, ABC mix solution from VECTASTAIN ABC kit (Vector) for 1 h, and tyramide dissolved in 0.1 M borate were applied for 10 min with stringent washings between the incubations. Streptoavidin Alexa Fluor 594 (Thermo Fisher Scientific) was then applied for 1 h, followed by DAPI and coverslip. For the cortical layer-specific markers (SATB2, CTIP2, and TBR1), since CTIP2 was clearly specific to Layer V, we defined Layer II–IV as SATB2-stained area bounded by CTIP2-positive Layer V, and Layer VI as TBR1-positive area bounded by CTIP1-positive area. The terminal deoxynucleotidyl transferase dUTP nick end labeling (TUNEL) assay was performed according to the manufacture's protocol using ApopTag Fluorescein *in situ* apoptosis Detection kit (Millipore). To combine immunofluorescence signals with TUNEL, TUNEL assays were performed first, followed by blocking, primary and secondary antibody incubations as described above.

Fluorescently stained sections were observed under a confocal laser scanning microscope (Nikon A1RGaAsP inverted microscope) or Nikon-Ti-E 90i upright widefield. Images were processed and analyzed using NIS Elements software (Nikon). For the quantification of OLIG2, GLUT1, NF-H, CD68, C3AR, SATB2, CTIP2, TBR1, DLX5, CALR, CALB, IBA1, TUNEL, NF-kB p65, Ki67-positive cells, the General Analysis (GA) tool in NIS Elements software was used, and the cell number was counted as an average of three regions of interest (ROIs) images captured with $20\times$ optical lens for OLIG2, DLX5, CALR, CALB, TUNEL, and Ki67 positive cells. CD68 positive cells were counted based on each section per animal, GLUT1 and NF-H positive area were measured by NIS Elements software (Nikon), and the number of p65-expressing cells was counted as a sum in three ROIs. For the measurement of cortical, ventricular, and white matter area, three comparable sagittal DAPI-stained sections per animal were picked, and average area was calculated with ImageJ software (NIH). ImageJ software was also used to estimate the CNP positive area in the strictly comparable sections at which the rostral migratory system from the subventricular zone to olfactory bulb is clearly visible. For characterizing C3AR-positive cells, images were captured at three ROIs in white matter and gray matter with $20\times$ optical lens, and the numbers of IBA1 positive round amoeboid-shaped macrophages and ramified-shaped microglia were independently manually counted. For the above quantification, the evaluator was blinded to the drug treatment options and genotype.

In situ hybridization (RNAscope)
RNAscope *in situ* hybridization was performed according to the manufacture's protocol of RNAscope Multiplex Fluorescent v2 Assay (Advanced Cell Diagnostics). Briefly, slides with 12-µm-thick cryosections were washed in PBS for 5 min, and hydrogen peroxide solution was incubated for 10 min. Slides were then performed target retrieval in Target Retrieval Reagent at 95°C for 5 min, briefly washed in nuclease-free water for 10 s, moved into 100% ethanol for 3 min, and dried completely. After application of Protease III for 15 min at 40°C, a combination of the probes for purinergic receptor P2Y, G-protein coupled, 12 (*P2ry12*; NM_027571.3, catalog #317601) mRNA, *Ccr2* (C-C motif chemokine receptor 2; NM_009915.2, catalog #501681) mRNA, *Mcp-1* (NM_011333.3, catalog #311791), and *Tmem119* (NM_146162.2, catalog #472901) mRNA were hybridized for 2 h at 40°C in a HybEZ oven. After stringent wash in wash buffer and signal amplification steps, TSA plus Cyanine three or TSA Plus Cyanine 5 (PerkinElmer) were incubated for 30 min at 40°C, and horseradish peroxidase signals of each channel were developed. To combine RNAscope signals with immunofluorescence, slides were further washed after the development of RNAscope fluorophore signals, followed by blocking, primary and secondary antibodies

Table 1. Primers used for qRT-PCR experiments

Gene	Forward primer (5′—3′)	Reverse primer (5′—3′)	GenBank #
Mcp-1	TAAAAACCTGGATCGGAACCAAA	GCATTAGCTTCAGATTTACGGGT	NM011333
Tnf-α	CCTGTAGCCCACGTCGTAG	GGGAGTAGACAAGGTACAACCC	NM013693
Tlr-4	AAATGCACTGAGCTTTAGTGGT	TGGCACTCATAATGATGGCAC	NM021297
Hmox-1	GATAGAGCGCAACAAGCAGAA	CAGTGAGGCCCATACCAGAAG	NM010442
C3ar	TCGATGCTGACACCAATTCAA	TCCCAATAGACAAGTGAGACCAA	NM009779
Cd86	TGTTTCCGTGGAGACGCAAG	TTGAGCCTTTGTAAATGGGCA	NM019388
Cd40	TGTCATCTGTGAAAAGGTGGTC	ACTGGAGCAGCGGTGTTATG	NM170702
Arg1	CTCCAAGCCAAAGTCCTTAGAG	AGGAGCTGTCATTAGGGACATC	NM007482
Il4	GGTCTCAACCCCCAGCTAGT	GCCGATGATCTCTCTCAAGTGAT	NM021283
Gapdh	AGGTCGGTGTGAACGGATTTG	TGTAGACCATGTAGTTGAGGTCA	NM008084

incubation as described above. Pictures of slides with RNAscope *in situ* hybridization were captured under Keyence BZ-X810.

Synapse quantification
Synapses were quantified according to the protocol previously described (Shi et al., 2015) with modification. Brain tissues were sectioned at 12-µm thickness. Three ROIs in comparable sections per animal were used for immunostaining with antibodies against the presynaptic protein, anti-guinea pig VGLUT2 (1:1000, Millipore, AB2251-I) and the postsynaptic protein anti-rabbit HOMER1 (1:1000, Millipore, ABN37). The stained sections were imaged within 5 d of staining with Nikon A1R inverted microscope with $100\times$ oil objective lens with Nyquist focusing with pinhole 1.2 AIU, gaining 0.11 µm/pixel resolution. Z-stack images of 21 serial optical frames (0.25-µm step, 5-µm total thickness from the surface of the tissue) were captured from the sensorimotor cortex in the area of Layer II/III and Layer IV. The denoised and deconvolved images were imported to Imaris 9.6.0 software, and 3D reconstructed images were analyzed with surface and spot creation algorithm. HOMER1$^+$ postsynaptic domain was defined with diameter of largest sphere at 0.6 µm, seed points diameter 0.5 µm with signal intensity threshold 28%. VGLUT2$^+$ presynaptic protein was defined with diameter of largest sphere at 0.6 µm, seed points diameter 0.6 µm, with signal intensity threshold 15%. Iso-surface was created for HOMER1 and was used to mask VGLUT2 signal, to define overlapping volume. Synapses were determined using the spot detection algorithm with the shortest distance calculation and with the source channel of the masked channel. XY diameter of 0.3 µm and PSF-elongated Z diameter of 0.8 µm were applied, and the spots detected with a threshold 25–30% were defined as synapses.

Behavioral test
The following battery of tests were performed in two phases so that the neonatal reflex and locomotion test would be robust. Animals were marked with Animal Markers (Stoelting) and the tip of the tails were clipped instead of toes for genotyping. The litter size was culled down to five or six pups per litter at P3, to minimize the testing variability and biases. For all the tests, animals were moved to a quiet testing room with dams and habituated for 1 h, and testing was performed in the morning. In phase 1, we performed the surface righting reflex (P4, P6, P8), the grasp reflex (P4, P6, P8), the negative geotaxis test (P4, P6, P8), and a swim test (P8) in untreated WT ($n = 12$) and *prh* animals ($n = 18$ for P4 and P6, $n = 15$ for P8 as three *prh* mutants died between P6 and P8). After observing a robust phenotype in untreated *prh* compared with WT animals, we performed a swim test at P8 for phase 2 in animals with vehicle or bindarit injections (daily from P4 to P7) in WT and *prh* ($n = 12$ for veh-WT, $n = 13$ for veh-*prh*, $n = 8$ for bin-*prh*). Reflex tests were video recorded at 30 frames/s and swim tests were recorded with a high-speed camera (120 frames/s). All data were analyzed by two independent investigators blinded to both genotype (WT vs *prh*) and/or drug treatment (vehicle vs bindarit).

Surface righting reflex
Performed at P4, P6, and P8. Pups were placed on their backs on a cotton sheet over a heat pad (37°C), held for 5 s, and released. The time it takes the pup to return to prone position was recorded and average time

was calculated from a total of three trials. Maximum time of 1 min was given for each trial.

Grasp reflex
Performed at P4, P6, and P8. Pups were held by the scruff of the neck gently, and each paw was stroked with a paper clip. Each paw was individually evaluated for either presence or absence of the grasping reflex.

Negative geotaxis test
Performed at P4, P6, and P8. Pups were placed with their heads pointing downward on a 30 degree inclined corrugated cardboard ramp, held for 5 s, and released. The angle and ramp material were chosen to minimize falling from the surface while inducing upward turning. The time taken by animal to turn and face upward was recorded, and the average time was calculated from a total of three trials. Maximum of 1 min was given for each trial. If the mice fell or did not attempt, this was also noted and excluded from the time calculation (Tsai et al., 2013; Feather-Schussler and Ferguson, 2016).

Swim test
The swim test was performed at P8, considering that pups start to use all limbs at an early postnatal age (Adencreutz and Hau, 2008). Pups were placed in a transparent beaker (1000 ml for phase 1, 2000 ml for phases 2 and 3) containing water at a depth of 15 cm and maintained at 34–36°C (Adencreutz and Hau, 2008). The movement of forelimbs and hindlimbs were captured for 10 s from the bottom where transparent acryl board and the video camera with a slow-motion spec at 120 fps was placed. After the first trial, the mice were briefly dried and warmed, and put into the water for the second trial within 20 s. Frequency of left-right hindlimbs alternation per second was calculated once pups began the first left-right coordination. Forelimb movements were not quantified because of their use in changing the swim direction and less consistent left-right alternate movements compared with the hindlimbs.

Statistical analysis
All values are expressed as the mean ± SEM. Statistical computation of group differences among two drug treatment groups (vehicle and bindarit) and two genotype groups (WT and *prh*) was performed using a two-way ANOVA with Tukey's *post hoc* test for multiple comparisons. Repeated measures of ANOVA with Sidak's *post hoc* test was performed for behavioral tests with multiple time points. Survival data were analyzed using the log-rank procedure of Kaplan–Meier survival analysis. Body weights and head sizes normalized to body weights were analyzed by repeated measures using a two-way ANOVA, followed by Tukey's *post hoc* test. The differences between two groups were compared with the Student's *t* test. $p < 0.05$ was generally considered to be statistically significant, while $p < 0.01$ was used for NanoString pathway analysis. All statistical computations were performed using GraphPad Prism.

Results

Activation of myeloid cells in the *prh* hydrocephalic mouse brains

We found that several proinflammatory cytokine mRNAs that are elevated in other hydrocephalus models (Lattke et al., 2012; Kurt et al., 2010; Karimy et al., 2017; Zhang et al., 2018a) are also upregulated in the P8-P10 *prh* hydrocephalic brains; *Mcp-1* (**$p = 0.0057$), *Tnf-α* (*$p = 0.019$), *Toll-like receptor 4* (*Tlr-4*; *$p = 0.0310$), and *Heme oxigenase-1* (*Hmox-1*; *$p = 0.0464$, $n = 5$–6 in each group; Fig. 1A). Among these cytokines, *Mcp-1* mRNA expression level was well correlated with the severity of ventriculomegaly calculated using the contralateral hemisphere ($R^2 = 0.7385$, $n = 12$; Fig. 1B). In order to comprehend the neuroinflammatory signature and identify active inflammatory cascades in the developing brain with hydrocephalus, we next performed nCounter Mouse Inflammatory panel assay using cerebral cortical RNAs ($n = 6$ in each group). Among 250 inflammatory genes tested, we found 28 genes upregulated
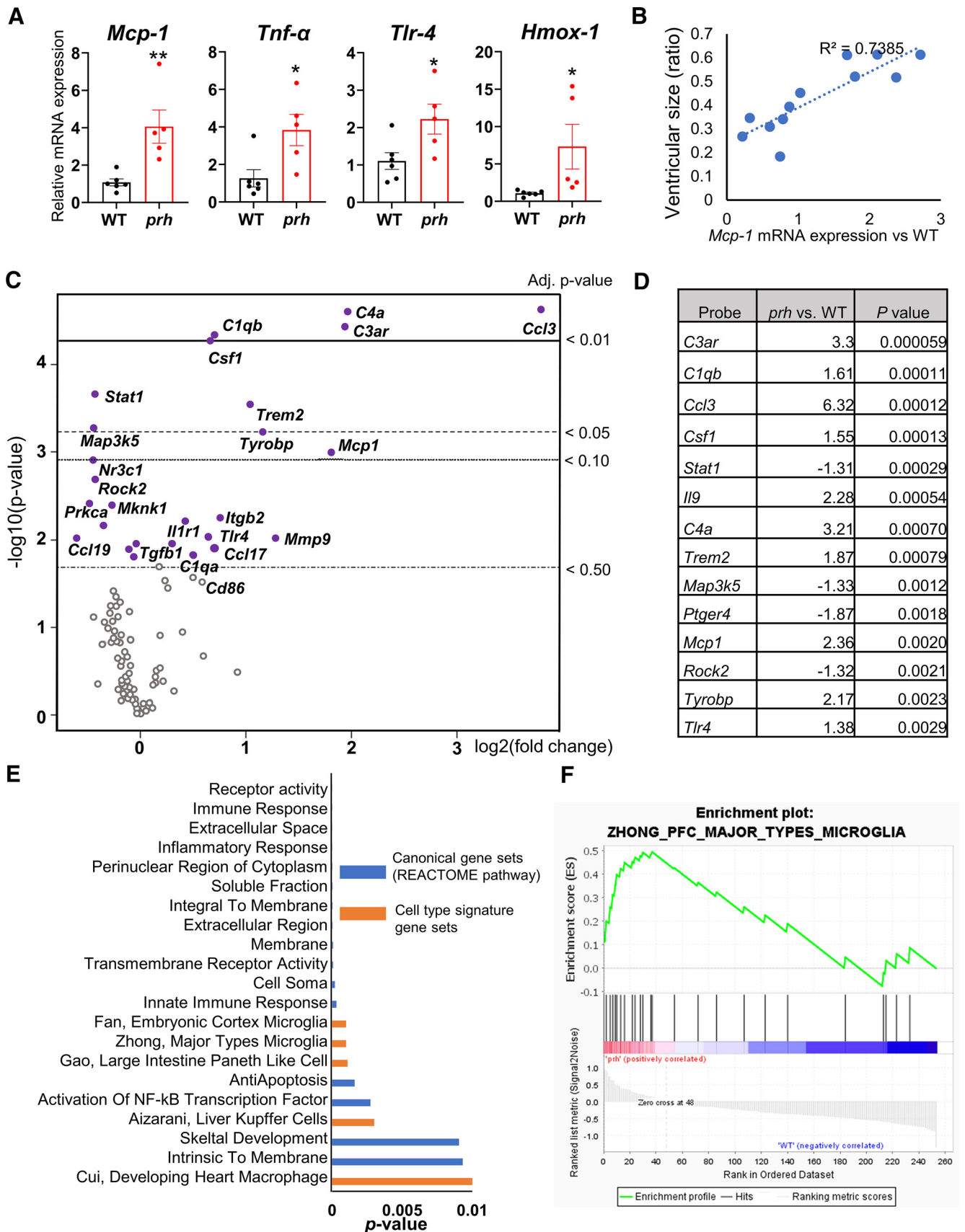
Figure 1. Inflammation and myeloid cell involvement in *prh* hydrocephalic mouse brains. *A*, The *Mcp-1* (**$p = 0.0057$), *tumor necrosis factor* (*Tnf*)-α (*$p = 0.019$), *Tlr-4* (*$p = 0.0310$), *Hmox-1* (*$p = 0.0464$) mRNA expression relative to housekeeping gene *Gapdh* mRNA are significantly upregulated in *prh* relative to that in WT mouse brains (without treatment, P8–P10, Student's *t* test, $n = 5$–6 in each group). *B*, *Mcp-1* mRNA in nontreated *prh* is well correlated with the severity of ventricular size ($R^2 = 0.7385$, $n = 12$). *C*, Volcano plot of differentially expressed genes (DEGs) in P8 *prh* brains relative to WT (data based on $n = 6$ in each group). Adjusted *p* value < 0.5 is shown. *D*, DEGs with nominal *p* value < 0.01. *E*, nSolver pathway

and 19 genes downregulated in *prh,* including upregulation of *Ccl3, C3ar, Tyrobp, Trem2, C1qb, C1qa, Tlr4,* and *Cd86* [significantly differentially expressed genes with adjusted *p* value < 0.50 (Fig. 1C); genes with nominal $p < 0.01$ (Fig. 1D)]. nSolver pathway analysis identified 16 gene sets upregulated in *prh,* including activation of NF-kB transcription factor ($p = 0.0027$) and innate immune response ($p = 0.00031$; Fig. 1E, shown in blue). Also, gene enrichment analysis with cell type signature gene sets (C8) identified 5 gene sets significantly enriched in *prh* (False discovery rate q-value $< 25\%$, nominal *p* value < 0.01; Fig. 1E, shown in orange), including developing heart macrophages ($p < 0.001$, Cui et al., 2019), major types of microglia ($p < 0.001$; Zhong et al., 2018; enrichment plot shown in Fig. 1F), and embryonic cortex microglia ($p < 0.001$; Fan et al., 2018). These microglia-signature and macrophage-signature gene sets annotated overlapping genes, most of which were also identified to be significantly upregulated in *prh* mutants as the volcano plot showed, along with *Mcp-1* (Fig. 1C). These results suggested that mononuclear myeloid cells are the major players in the inflammatory response in *prh,* which is in accordance with previous findings in other neonatal hydrocephalus models cited above.

The pharmacokinetics of subcutaneously administered bindarit in neonatal mice
In order to modulate the proinflammatory response, we evaluated the pharmacokinetics of a potent anti-inflammatory drug, bindarit, which inhibits myeloid cell activation by blocking inflammation-mediated nuclear translocation of NF-kB (Mora et al., 2012), in neonatal WT and *prh* mice. A single dose subcutaneous administration of bindarit (molecular weight 324.4 g/mol, 100 mg/kg) in P7 WT mice reached the brain within 3 h (85,400 ng/g = 263 μM) and was gradually metabolized, to 17,800 ng/g (54.9 μM) at 24 h (Fig. 2A). As bindarit significantly suppresses *Mcp-1* mRNA in cultured microglia at 50 μM (Ge et al., 2012), this result indicated successful delivery of bindarit to the neonatal mouse brain and maintained concentrations above the target level for 24 h. Once-a-day injections for four consecutive days did not change the tissue level of bindarit in the brain at 24 h from the last injection compared with that of a single injection (Fig. 2B), which indicated that bindarit does not accumulate in the brain after daily dosing and thus justifies the effectiveness of once-a-day injections of bindarit at 100 mg/kg. Furthermore, neither increasing the dose of bindarit to 200 mg/kg nor the *prh* genotype altered the bindarit level in the brain and the liver at 24 h (Fig. 2C). Therefore, the *prh* genotype did not affect the brain availability of bindarit at P7, as compared with WT.

Bindarit attenuates edematous swelling of white matter but only slightly improves ventricular enlargement in *prh* mutants
We performed daily injections of bindarit (100 mg/kg, s.c.) in WT and *prh* mice from P4 through P7 and evaluated tissue area of gray matter (i.e., total cerebral cortical area excluding white matter), white matter, and lateral ventricles measured from strictly comparable, DAPI-stained low power field pictures. The

←

analysis based on REACTOME pathway identified 16 gene sets upregulated in *prh* (blue), and gene enrichment analysis with cell type signature gene sets (C8) identified five gene sets enriched in *prh* (orange; false discovery rate $< 25\%$, nominal *p* value < 0.01). ***F,*** Enrichment plot of major types of microglia gene sets identified the positive enrichment of microglial genes in *prh* compared with WT.

enlarged lateral ventricle size in vehicle-treated (veh-) *prh* ($\dagger\dagger\dagger\dagger p < 0.0001$ to veh-WT) was significantly and mildly attenuated by bindarit treatment (**$p = 0.0083$), still exhibiting significantly larger ventricles in bindarit-treated (bin-) *prh* relative to WT ($\dagger\dagger\dagger\dagger p < 0.0001$ to veh-WT; Fig. 2D, middle). The white matter was edematous and swollen in veh-*prh* relative to WT ($\dagger\dagger\dagger\dagger p < 0.0001$ to veh-WT; Fig. 2D, right, E), reinforcing the finding that there is considerable neuroinflammation and tissue damage in the white matter of *prh* (Goulding et al., 2020). It is notable that this white matter swelling, because of edema, was dramatically improved in bin- *prh* (***$p = 0.0008$ compared with veh-*prh*, $n = 13$ in each group; Fig. 2D, right). The total gray matter size was comparable among all groups ($p = 0.800$ for genotype, $p = 0.468$ for drug, two-way ANOVA, $n = 13$ in each group; Fig. 2D, left). Survival (Fig. 2F), body weight (Fig. 2G), and head circumference (Fig. 2H) in *prh* were not improved with bindarit treatment.

Myelination and vascularization in *prh* white matter is improved with bindarit treatment
To characterize the impact of white matter edema in *prh* and its alleviation by bindarit in myelination, we performed immunohistochemistry with two oligodendrocyte lineage cell-specific markers. The pan-oligodendrocyte lineage marker, OLIG2, showed the significantly reduced density of total oligodendrocytes in veh-*prh* ($\dagger\dagger\dagger\dagger p < 0.0001$ compared with veh-WT) and it was rescued by bindarit treatment (*$p = 0.0385$ compared with veh-*prh*, $n = 12$–13 in each group), most likely reflecting the edematous change in the white matter (Fig. 3A). Interestingly, mature oligodendrocyte and myelination marker CNP (2′,3′-cyclic nucleotide 3′ phosphodiesterase) staining showed a significant reduction of myelination in veh-*prh* ($\dagger\dagger\dagger\dagger p < 0.0001$ compared with veh-WT), which was partially recovered in bin-*prh* (*$p = 0.0113$ compared with veh-*prh*, $n = 12$–13 in each group; Fig. 3B). These data indicate that bindarit treatment improves the maturation of oligodendrocytes and myelination in *prh* brains. To evaluate the axons adjacent to periventricular regions, NF-H staining was performed. It showed intact periventricular axon bundles even in veh-*prh* (Fig. 3C), implying that the observed myelin impairment precedes the axonal loss reported in neonatal hydrocephalus. Since the reduction of cerebral blood flow in white matter has been well documented in neonatal hydrocephalus patients (Shirane et al., 1992) and reduced vessel density in white matter has supported the finding (Jones et al., 1991), an endothelial cell marker GLUT1 staining was performed. It showed reduced vessel density in veh-*prh* compared with WT ($\dagger\dagger\dagger p < 0.0004$ compared with veh-WT), with significant recovery of vessel density in bin-*prh* (**$p = 0.0019$ compared with veh-*prh*, $n = 6$ in each group; Fig. 3D). The vessel density was also normalized to DAPI positive cells to adjust for the effect of the edematous swelling of the tissues, but it was still significantly decreased in the veh-*prh* ($\dagger p = 0.0219$ compared with veh-WT) and recovered with bindarit (*$p = 0.0253$ compared with veh-*prh*, graph not shown). These data demonstrate the protective effect of bindarit on white matter edema along with the improved myelination and preserved vascularization in the periventricular white matter in *prh* hydrocephalic brains.
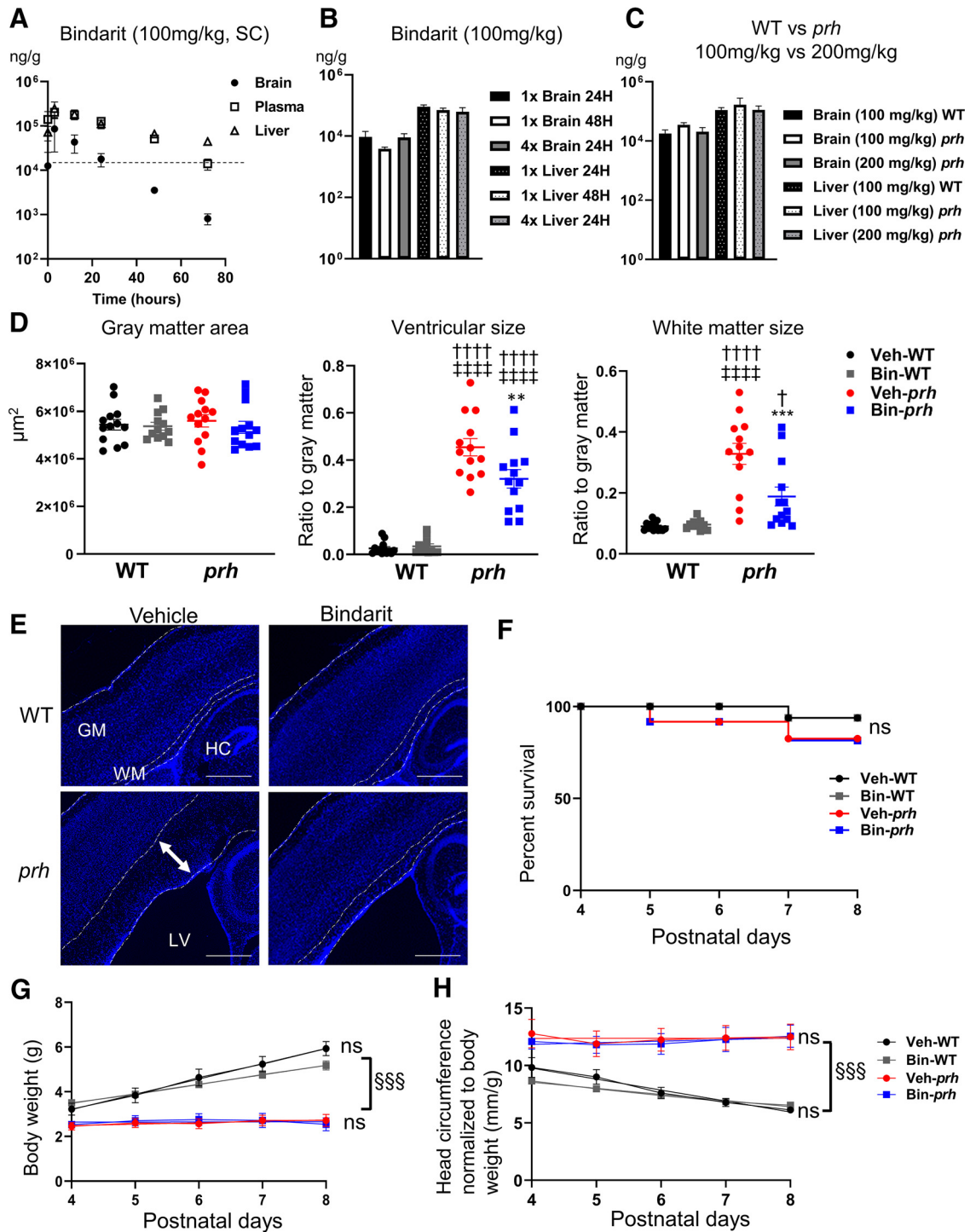
Bindarit suppresses CD68^{+}-activated myeloid cell infiltration and *Mcp-1* expression in the periventricular white matter
We next evaluated myeloid cell activation in *prh* brains. Consistent with our previous reports (Emmert et al., 2019;

Figure 2. Pharmacokinetics of bindarit and its effect on ventricular and white matter enlargement. ***A***, Tissue concentration of bindarit in the brain, plasma, and liver at 0, 3, 12, 24, 36, and 72 h after the subcutaneous injection. Dotted line indicates 16,620 ng/g as effective tissue concentration. ***B***, Tissue concentration of bindarit in brain and liver, 24 or 48 h after the single, once-a-day injection (1×) and once-a-day injection for four consecutive days (4×). ***C***, Tissue concentration of bindarit in brain and liver 24 h after the single injection of 100 or 200 mg/kg in either WT or *prh* genotype. ***D***, Tissue area size of gray matter (total cerebral cortical area excluding white matter), ventricular size relative to gray matter [††††$p < 0.0001$ to vehicle-treated (veh-) WT, ‡‡‡‡$p < 0.0001$ to bindarit-treated (bin-)WT, **$p = 0.0083$ to veh-*prh*], and white matter size relative to gray matter (†$p = 0.0274$, ††††$p < 0.0001$ to veh-WT, ‡‡‡$p < 0.0001$ to bin-WT, ***$p = 0.0008$ to veh-*prh*) measured from DAPI-stained low power field pictures (two-way ANOVA followed by Tukey's test, $n = 13$ in each group). ***E***, Low power field pictures of DAPI-stained animals. Double-headed arrow in veh-*prh* shows the swollen white matter (scale bars: 500 μm). GM, gray matter; WM, white matter; HC, hippocampus. ***F***, Kaplan–Meier survival plot shows the survival rate of veh-WT and bin-WT are 93%, and veh-*prh* and bin-*prh* are 87.5% at P8 [nonsignificant (ns) in 4 groups]. ***G***, Body weight analysis demonstrates that *prh* exhibit less weight growth compared with WT (§§§$p < 0.001$, *prh* vs WT) and no significant (ns) difference by treatment (repeated measures two-way ANOVA followed by Tukey's test, $n = 8$–10). ***H***, Head circumference as a sum of the three directions (top-bottom, left-right, rostral-caudal, mm) normalized to body weight gradually declines in WT as they grow, but it stays relatively large in *prh* (§§§$p < 0.001$, *prh* vs WT), with no significant (ns) difference by drug treatment (repeated measures two-way ANOVA followed by Tukey's test, $n = 8$–12).
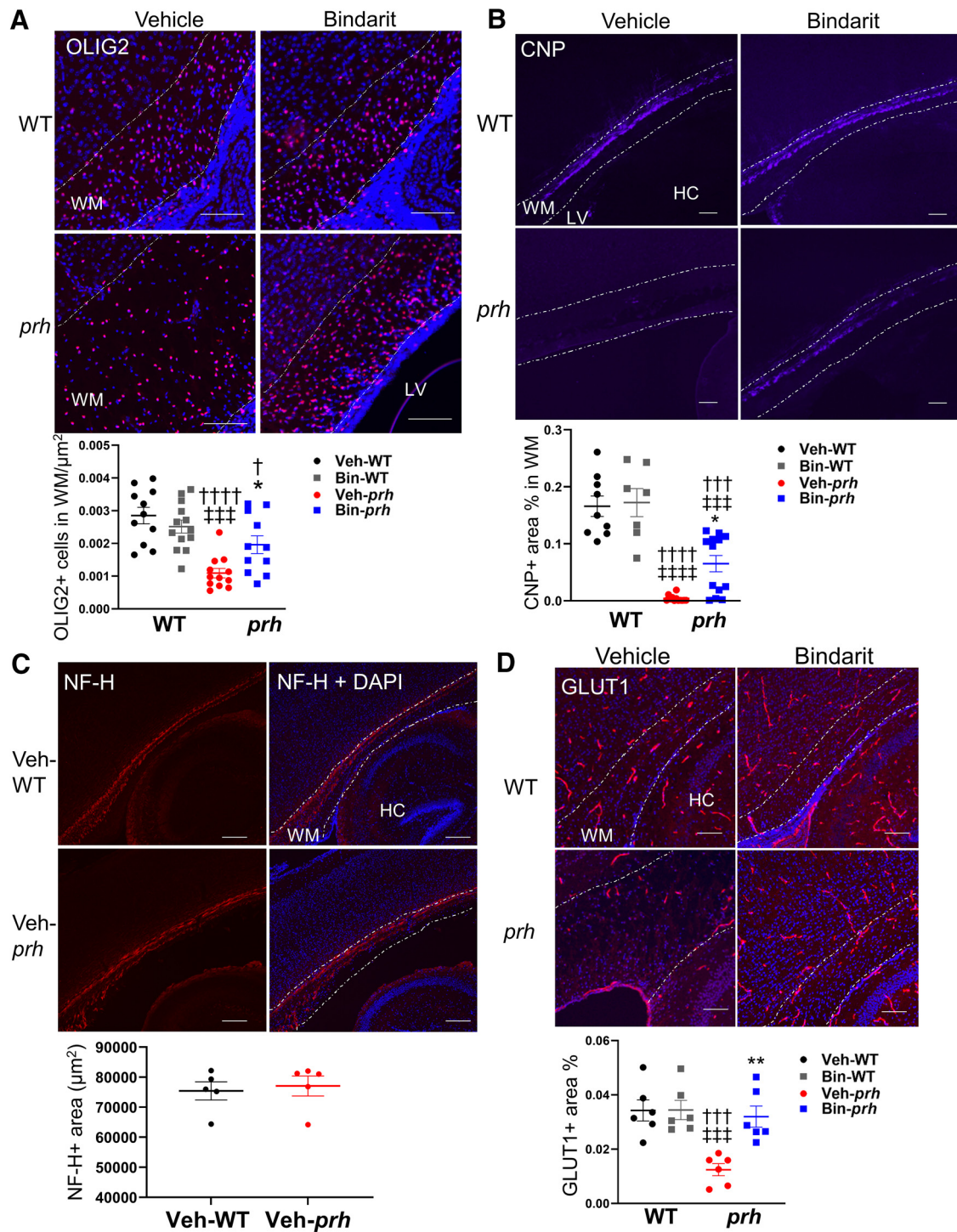
Figure 3. Myelination and vascularization in *prh* white matter with bindarit treatment. *A*, Number of pan-oligodendrocyte lineage marker OLIG2$^+$ cells per WM shows reduced oligodendrocyte density in veh-*prh* and improvement in bin-*prh* (†$p = 0.0367$, ††††$p < 0.0001$ vs veh-WT, ‡‡‡$p = 0.001$ vs bin-WT, *$p = 0.0385$ vs veh-*prh*; two-way ANOVA followed by Tukey's test, $n = 12$–13 in each group; scale bars: 100 μm). *B*, The mature myelination marker CNP positive staining area % in WM shows significant reduction of myelination in veh-*prh* and partial recovery in bin-*prh* (†††$p = 0.0001$, ††††$p < 0.0001$ vs veh-WT, ‡‡‡$p = 0.0002$, ‡‡‡$p < 0.0001$ vs bin-WT, *$p = 0.0133$ vs veh-*prh*; two-way ANOVA followed by Tukey's test, $n = 10$–13 in each group; scale bars: 100 μm). *C*, Neurofilament-labeled axons (NF-H) positive area (μm^2) in WM shows no significant difference between veh-WT and veh-*prh* ($p = 0.7244$; Student's *t* test, $n = 5$ in each group; scale bars: 200 μm). *D*, Endothelial cell marker, GLUT1 positive staining area per WM (%) shows reduced vascular densities in veh-*prh* and significant recovery in bin-*prh* (†††$p = 0.0004$ vs veh-WT, ‡‡$p = 0.0001$ vs bin-WT, **$p = 0.0019$ vs veh-*prh*; two-way ANOVA followed by Tukey's test, $n = 6$ in each group; scale bars: 100 μm). WM, white matter; LV, lateral ventricles; HC, hippocampus.

Goulding et al., 2020), there was a vast accumulation of CD68$^+$-activated myeloid cells (Boer et al., 2006; Van Vliet et al., 2012; Tanaka et al., 2013) in the periventricular white matter of the veh-*prh*, whereas there were very few CD68$^+$ cells in veh-/bin-WT and remarkably, bin-*prh* cortex (Fig. 4A). We found that daily bindarit injections suppressed activated myeloid cell accumulation in the *prh* mutant brain (**$p = 0.0040$, $n = 7$ in each group; Fig. 4A, graph) coincided with the reduced white matter
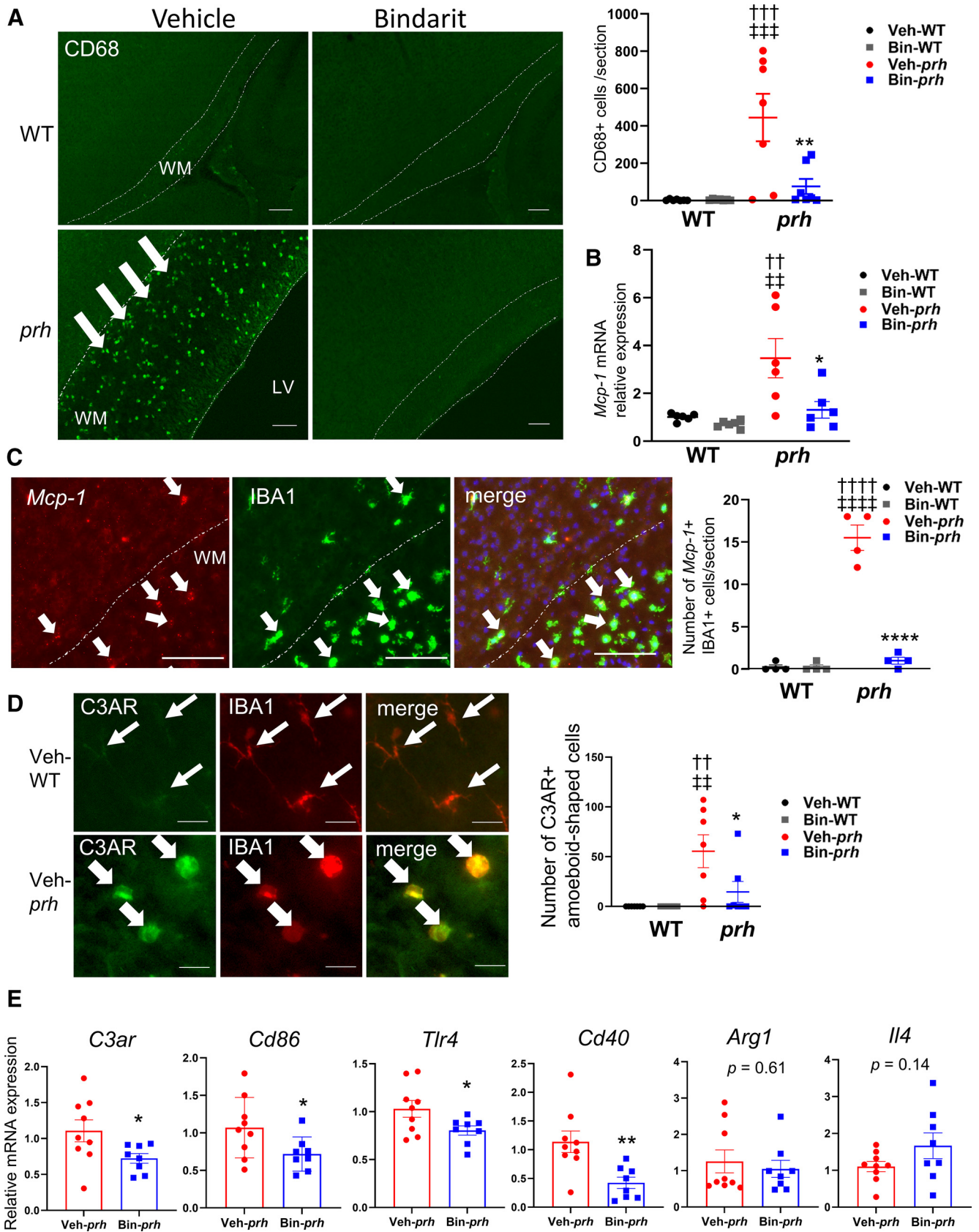
Figure 4. Bindarit's effect on myeloid cell activation in the periventricular white matter. ***A***, CD68^{+}-activated myeloid cells are rarely seen in veh-WT and bin-WT at P8, but significantly increased in white matter (WM) of veh-*prh*, which is significantly suppressed in bin-*prh* (†††$p < 0.0001$ vs veh-WT, ‡‡‡$p < 0.0001$ vs bin-WT, **$p = 0.0040$ vs veh-*prh*; two-way ANOVA followed by Tukey's test, $n = 6–7$ in each group; scale bars: 100 μm). ***B***, *Mcp-1* mRNA relative to *Gapdh* mRNA is upregulated to 3.47 ± 0.82 times relative to veh-WT in veh-*prh* and is significantly suppressed in bin-*prh* (†††$p = 0.0047$ vs veh-WT, ‡‡‡$p = 0.0016$ vs bin-WT, **$p = 0.0135$ vs veh-*prh*; two-way ANOVA followed by Tukey's test, $n = 6$ in each group; scale bars: 100 μm). ***C***, *Mcp-1 in situ* hybridization shows exclusive *Mcp-1* mRNA expression by amoeboid-shaped IBA1^{+} myeloid cells in the periventricular WM and lower cortical layers of veh-*prh*,

injury described above (Figs. 2D, 3). *Mcp-1* mRNA, the primary downstream target of bindarit, was 3.47 ± 0.82 times higher in the veh-*prh* brain than veh-WT (††$p = 0.0055$), but was significantly suppressed after bindarit treatment (1.31 ± 0.35 times to the veh-WT, $p = 0.9979$ for bin-*prh* vs veh-WT, **$p = 0.0164$ for bin-*prh* vs veh-*prh*, $n = 6$; Fig. 4B). To identify *Mcp-1*-expressing cells, we performed RNAscope *in situ* hybridization and found exclusive *Mcp-1* expression by amoeboid-shaped IBA1^{+} myeloid cells in the *prh* mutants' periventricular white matter and deep portions of the cortical plate (Fig. 4C), but not by astrocytes/pericytes/neurons, and at a negligible level in endothelial cells (data not shown). The number of *Mcp-1* mRNA-expressing IBA1^{+} cells in *prh* brains was significantly reduced by bindarit treatment (Fig. 4C), in accordance with the reduction in the number of amoeboid-shaped myeloid cells. We further analyzed the cellular expression pattern of the highly upregulated gene, *C3ar*, detected in nontreated *prh* animals (Fig. 1). The complement system is a key regulator of innate immunity and C3AR, a G-protein-coupled receptor for C3A complement protein signaling, has been described as a central mediator of microglial activation in response to a variety of CNS diseases (Gasque et al., 1998; Zhang et al., 2020). We found that C3AR protein is almost solely expressed in the IBA1^{+} cells in both WT and *prh* brains (Fig. 4D). In WT, the C3AR signal was weakly expressed on the ramified-shaped homeostatic microglia in gray matter, whereas C3AR was strongly expressed in the IBA1^{+} amoeboid cells in veh-*prh* coinciding with *C3ar* mRNA upregulation in nontreated *prh* brains (Fig. 1C,D). Importantly, the number of C3AR-expressing IBA1^{+} amoeboid cells was significantly reduced by bindarit treatment (Fig. 4D, graph). Quantitative RT-PCR showed that, in addition to *Mcp-1*, the inflammatory genes related with microglia/macrophage activation including *C3ar*, *Cd86*, and *Tlr4*, as well as the proinflammatory microglia/macrophage activation (= classical activation; M1) marker *Cd40* mRNA (Liu et al., 2013; Zhou et al., 2017) were significantly suppressed in bin-*prh* brains (Fig. 4E). In contrast, expression levels of the anti-inflammatory microglial/macrophage activation (= alternative activation; M2) markers *Arginase 1* (*Arg1*) and *Interleukin 4* (*Il4*; Cherry et al., 2014; Abdelaziz et al., 2020), were not differentially expressed in nontreated *prh* relative to WT (data not shown), and were not changed by bindarit treatment (Fig. 4E). These results suggest that bindarit suppresses proinflammatory myeloid cells activation in the hydrocephalic brain.

Impaired development of cortical neurons in the *prh* mutant and the ameliorative effect of early postnatal bindarit treatment

In the early postnatal mouse cerebral cortex, postmitotic pyramidal neurons extend exuberant projections as callosal (Fame et al.,

---

and significant suppression in bin-*prh* (††††$p < 0.0001$ vs veh-WT, ‡‡‡$p < 0.0001$ vs bin-WT, ****$p < 0.001$ vs veh-*prh*; two-way ANOVA followed by Tukey's test, $n = 4$ in each group; scale bars: 100 μm). **D**, Complement receptor C3AR is weakly expressed in IBA1^{+} ramified microglia in gray matter of veh-WT (top) but is strongly expressed in amoeboid-shaped IBA1^{+} cells in WM of veh-*prh* (bottom). Number of C3AR-expressing amoeboid-shaped IBA1^{+} cells is suppressed in bin-*prh* relative to veh-*prh* (††$p = 0.0027$ vs veh-WT, ‡‡$p = 0.0027$ vs bin-WT, *$p = 0.0325$ vs veh-*prh*; two-way ANOVA followed by Tukey's test, $n = 7$ in each group; scale bar: 50 μm). **E**, Proinflammatory genes and cytokines involved in microglia/macrophage activation; *C3ar* (*$p = 0.0437$), *Cd86* (*$p = 0.0468$), *Tlr4* (**$p = 0.0052$), and *Cd40* (*$p = 0.0456$) mRNA are significantly suppressed in bin-*prh* compared with veh-*prh*, while alternative activation (M2) markers of microglia/macrophages *Arg1* ($p = 0.61$) and *Il4* ($p = 0.14$) are not changed by bindarit (Student's *t* test, $n = 8$–9 in each group).

2011) and collateral axons (Larsen and Callaway, 2006) as well as dendrites which characterize their "pyramidal" shape (Larsen and Callaway, 2006; Kroon et al., 2019). In neonatal hydrocephalus (Del Bigio, 2010) and its models, axonal damage along with hypomyelination in the periventricular white matter (Del Bigio et al., 1994, 1997) and reduced dendrite arborization (Kriebel et al., 1993; Harris et al., 1996) have been reported as developmental deficits. To characterize the benefit of bindarit in cortical development with neonatal hydrocephalus, we evaluated the cortical layer thickness and neuronal cell densities of upper layers (II–IV) and lower layers (V and VI) using layer-specific markers; SATB2 (II–IV), CTIP2 (V), and TBR1 (VI), respectively (Fig. 5A,B). The thickness of cortical Layer II through IV was significantly reduced in veh-*prh* (††††$p < 0.0001$ compared with veh-WT; Fig. 5A, bottom left, B, top left), which was partially, but significantly, improved in bin-*prh* (*$p = 0.011$ compared with veh-*prh*; Fig. 5A, bottom right, B, top left). Despite the improvement in Layer II–IV thickness, the cell density of SATB2^{+} neurons in these upper cortical layers were not significantly changed by bindarit treatment ($p = 0.6875$, bin-*prh* vs veh-*prh*, $n = 9$–10 in each group; Fig. 5B, bottom left). The CTIP2^{+} Layer V thickness was also reduced in *prh* brains (§§§$p = 0.0005$, *prh* vs WT), but was not recovered by bindarit ($p = 0.9869$, bin-*prh* vs veh-*prh*, $n = 9$–10 in each group; Fig. 5B, top middle). Conversely, TBR1^{+} Layer VI thickness, as well as the cell density of CTIP2/TBR1 positive Layer V/VI neurons, were not significantly reduced in *prh* brains and thus no effect of bindarit treatment was observed (Fig. 5B, bottom middle and right). These data indicate that (1) postnatal hydrocephalus does not reduce the neuronal cell densities at this stage (i.e., P8), and (2) cortical Layers II through V are vulnerable to the postnatal hydrocephalus insult leading to cortical thinning. However, Layers II–IV are more responsive to bindarit treatment, possibly because they are farther from the detrimental periventricular edema, and/or the later timing of active neuropil development than the lower layers (Kwan et al., 2012; Mukhtar and Taylor, 2018).

Embryonic neuronal cell migration and cortical thickness remains unchanged in *prh*, and no neuronal or astrocytic cell death is seen at P8

To rule out the possibility that the lack of ependymal ciliogenesis itself affects the embryonic neuronal cell migration and cortical development before hydrocephalus starts in the postnatal *prh* mouse, we performed cortical layers-specific analysis at E18 in WT and *prh* mutants. The thickness as well as neuronal cell density of each cortical layer was not significantly different between WT and *prh* brains ($n = 3$ in each group; Fig. 6A). Moreover, TUNEL staining at P8 showed no difference in apoptotic neuronal cell death between WT and *prh* cortex (Fig. 6B). TUNEL signal was also not observed in GFAP[+] astrocytes in WT or *prh* (Fig. 6C). These data confirmed normal embryonic neuronal cell migration and intact presence of the postnatal neuronal soma in *prh* neonatal hydrocephalus mice.

Excitatory synapse maturation is impaired in *prh* brains, and improved by bindarit treatment

To determine whether synaptic maturation is affected in the *prh* mutant cortex, we evaluated excitatory synapse numbers defined by an overlap between the presynaptic protein VGLUT2 (Fujiyama et al., 2001; Nahmani and Erisir, 2005) and postsynaptic protein HOMER1 (Gutierrez-Mecinas et al., 2016) at P8 in Layers II–IV of the somatosensory cortex. We focused on Layers II–III (Fig. 7A) and IV (Fig. 7B)
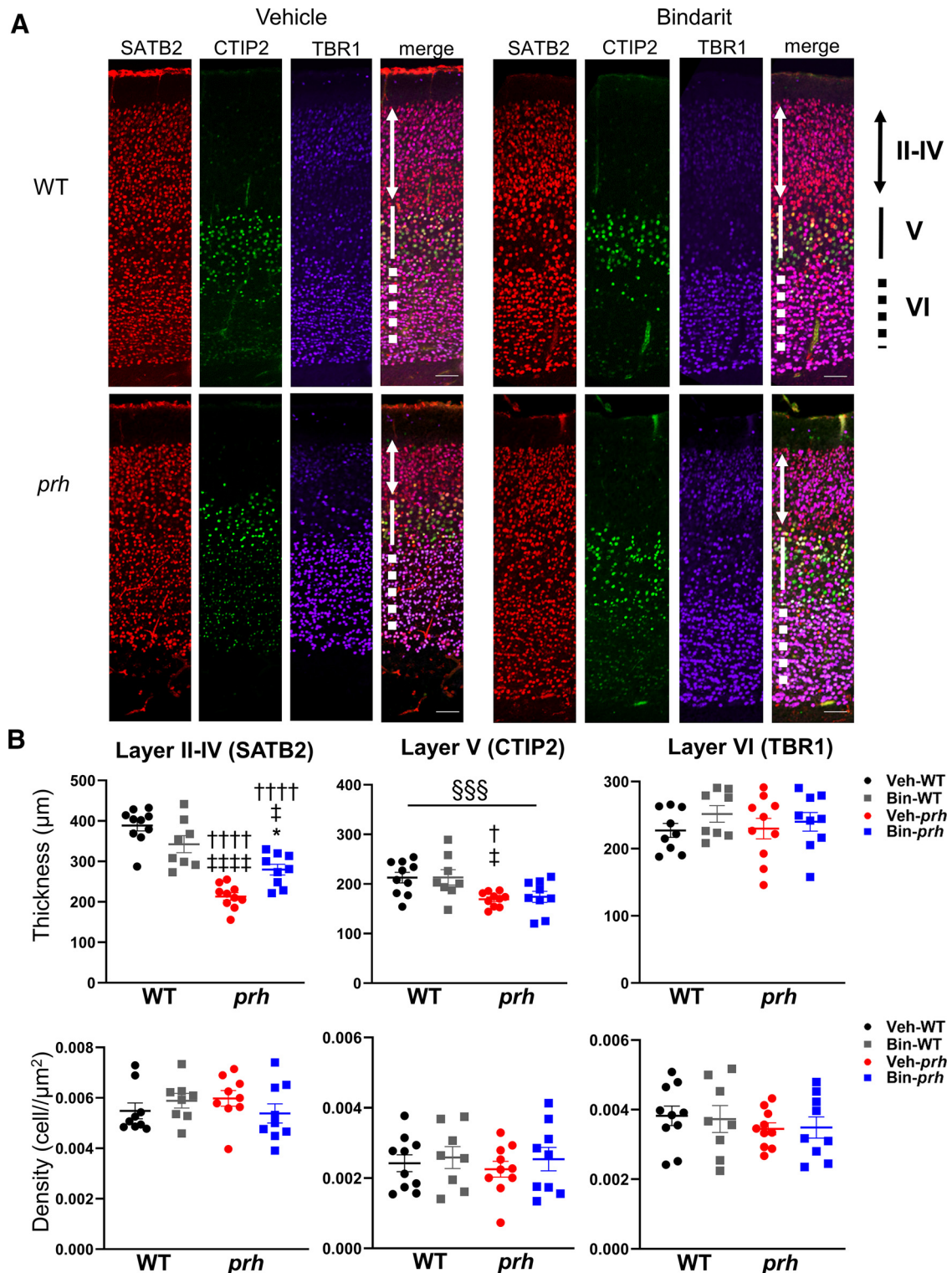
Figure 5. Impaired development of the cortical plate in the *prh* mutant and ameliorative effect by bindarit in Layers II–IV. ***A***, Cortical layer-specific markers SATB2 (II–IV), CTIP2 (***V***), and TBR1 (VI) are used to stain layer-specific cortical neurons in veh-/bin- WT and *prh* (scale bars: 100 μm). (***B***, top row) The thickness of cortical Layer II through IV is significantly reduced in veh-*prh*, and this defect is improved in bin-*prh* cortex (††††$p < 0.0001$ vs veh-WT, ‡$p = 0.0264$, ‡‡‡$p < 0.0001$ vs bin-WT, *$p = 0.0110$ vs veh-*prh*; two-way ANOVA followed by Tukey's test, $n = 9$–10 in each group; left top). ***B***, bottom row, The cell density of SATB2$^+$ neurons in cortical Layers II–IV are not significantly changed between groups (left bottom). CTIP2$^+$ cortical Layer V thickness is reduced in *prh* (§§§$p = 0.0005$, *prh* vs WT) and not recovered by bindarit ($p = 0.9869$, bin-*prh* vs veh-*prh*, two-way ANOVA followed by Tukey's test, $n = 9$–10 in each group; middle top). TBR1$^+$ Layer VI thickness (right top), as well as the cell density of CIPT2 (middle bottom)/TBR1 (right bottom) positive Layer V/VI neurons are not significantly altered in *prh* mutants.

separately because the neuronal constituents of each of these layers are largely distinct;. In the *prh* mutant, in line with the thinning of Layers II–IV (Fig. 5), we found reduced VGLUT2 (presynaptic) staining in the veh-*prh* cortex within

Layers II–III (††$p = 0.0089$ vs veh-WT; Fig. 7A, left) and Layer IV (†$p = 0.0103$ vs veh-WT; Fig. 7B, left). Similarly, HOMER1 (postsynaptic) staining was reduced in Layers II–III (†††$p = 0.0003$ vs veh-WT; Fig. 7A, middle) and Layer IV
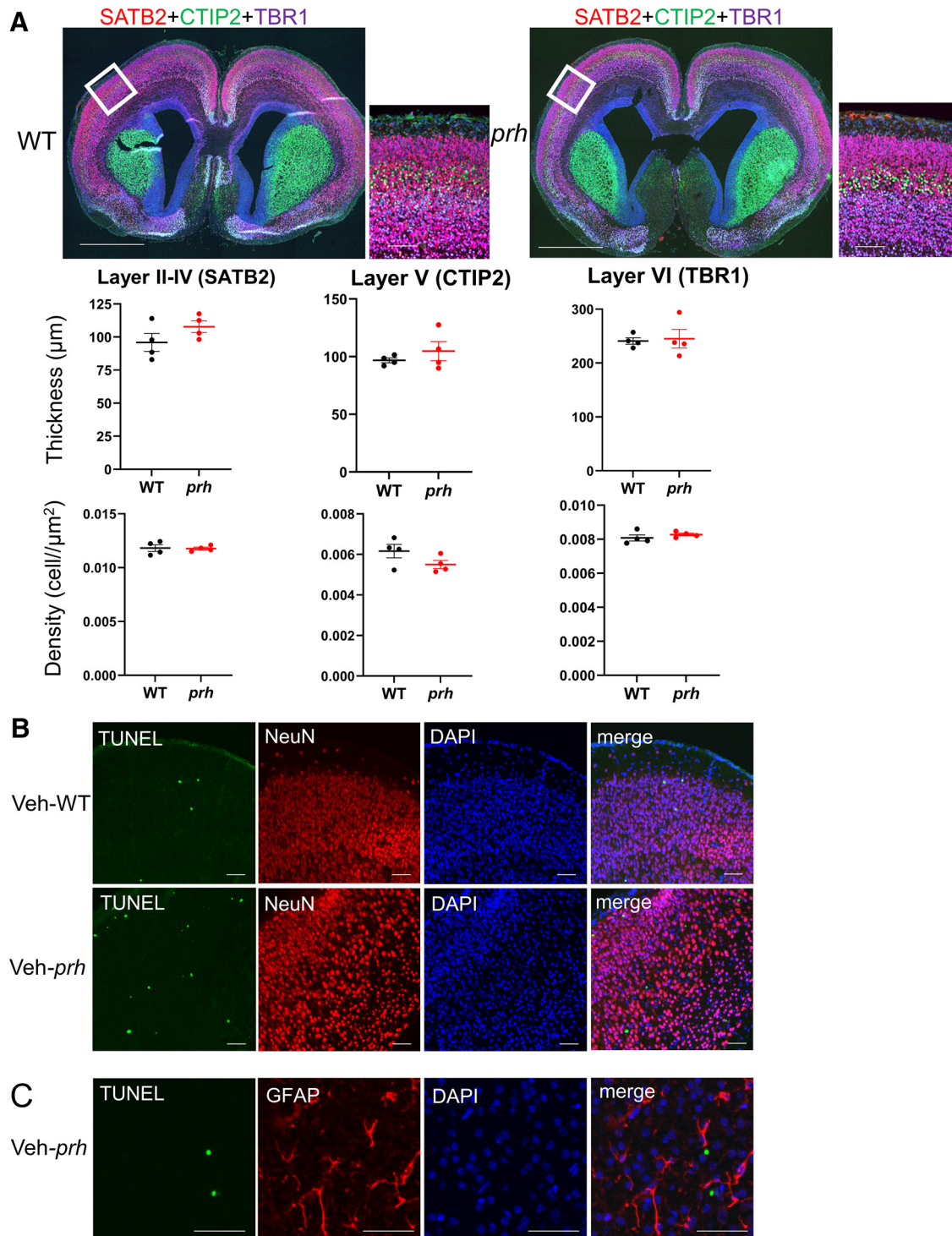
Figure 6. Normal neuronal migration and cortical plate thickness in the embryonic *prh* cortex, while no change in neuronal cell death at P8. ***A***, WT and *prh* brains at E18 stained with cortical layer-specific markers SATB2 (II–IV), CTIP2 (V), and TBR1 (VI) show no difference in thickness and neuronal cell density of each cortical layer between WT and *prh* (scale bars: 1000 μm for lower magnification pictures, 100 μm for higher magnification pictures, Student's *t* test, *n* = 3 in each group). ***B***, TUNEL/NeuN double staining at P8 in *prh* brains (top row, veh-WT; bottom row, veh-*prh*) shows more TUNEL-positive cells in veh-*prh* than veh-WT, but no change in apoptotic neuronal cell death (i.e., TUNEL/NeuN double staining) between WT and *prh* (scale bars: 100 μm, *n* = 3 in each group). ***C***, TUNEL/GFAP double staining at P8 in veh-*prh* brains shows no apoptotic astrocytic cell death (scale bars: 50 μm, *n* = 3).

($\dagger\dagger p = 0.0016$ compared with veh-WT; Fig. 7*B*, middle) of veh-*prh* cortex. Accordingly, mature synapses, as defined by co-labeling with VGLUT2 and HOMER1, were significantly reduced in both Layers II–III ($\dagger\dagger\dagger p = 0.0007$ vs veh-WT; Fig. 7*A*, right) and Layer IV [$\dagger\dagger\dagger\dagger p < 0.0001$ vs veh-WT; Fig. 7*B*, right; see also Movie 1 (veh-WT) vs Movie 2

(veh-*prh*) from Layer IV]. In Figure 5, we showed that bindarit treatment improved the thickness of Layers II–IV, and we hypothesized this could be because of enhanced neuronal maturation including synaptogenesis. Indeed, bindarit treatment was observed to improve synapse numbers in Layers II–III (*$p = 0.0317$ bin-*prh* vs veh-*prh*; Fig. 7*A*, right) and in Layer IV [****$p <$
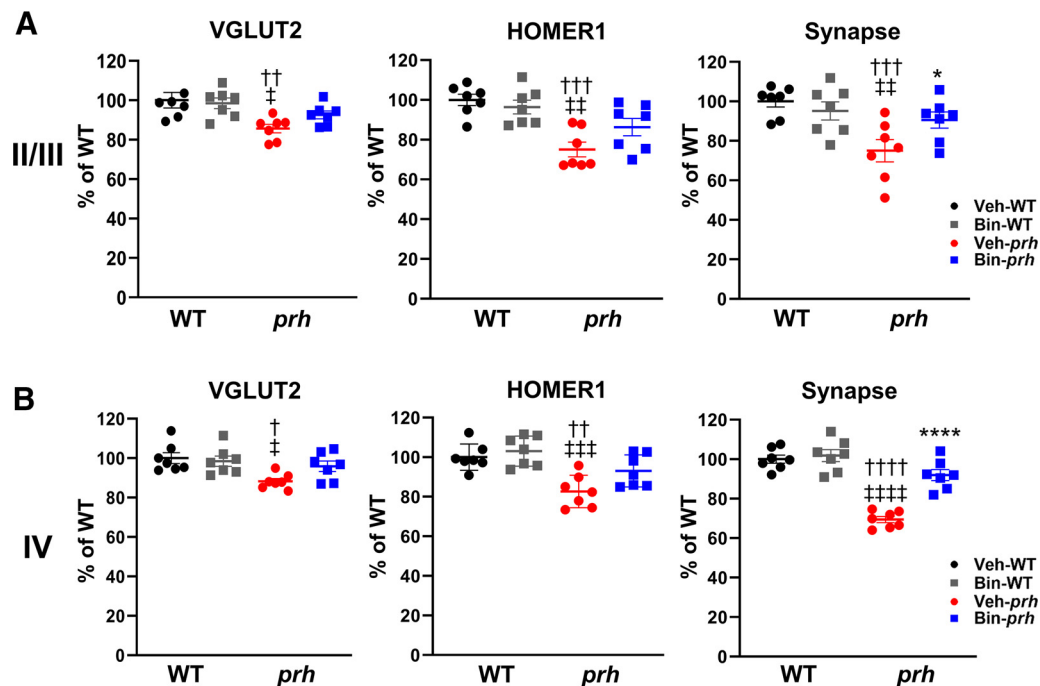
Figure 7. Impaired excitatory synapse maturation in *prh* brains and mitigation by bindarit treatment. Quantification of the numbers synapses defined by colocalization of the presynaptic protein VGLUT2, and the postsynaptic protein HOMER1 shows a reduction of the number of VGLUT2 (*A*, *B*, left; *A*: Layer II/III, ††$p = 0.0089$ vs veh-WT, ‡$p = 0.0215$ vs bin-WT; *B*: Layer IV, †$p = 0.0103$ vs veh-WT, ‡$p = 0.0297$ vs bin-WT) and HOMER1 (*A*, *B*, middle; *A*: †††$p = 0.0003$ vs veh-WT, ‡‡$p = 0.0019$ vs bin-WT; *B*: ††$p = 0.0016$ vs veh-WT, ‡‡‡$p = 0.0002$ vs bin-WT) in veh-*prh*, in both cortical Layer II/III and Layer IV. The numbers of synapses, identified as co-localization of VGLUT2 and HOMER1, shows a significant reduction in veh-*prh* in Layer II/III (*A*: right, †††$p = 0.0007$ vs veh-WT, ‡‡$p = 0.0052$ vs bin-WT) and Layer IV (*B*: right, ††††$p < 0.0001$ vs veh-WT, ‡‡‡$p < 0.0001$ vs bin-WT), which is significantly recovered in bin-*prh* (*A*: Layers II–III, *$p = 0.0317$, *B*: Layer IV, ****$p < 0.0001$ vs veh-*prh*; two-way ANOVA followed by Tukey's test, $n = 7$ in each group).
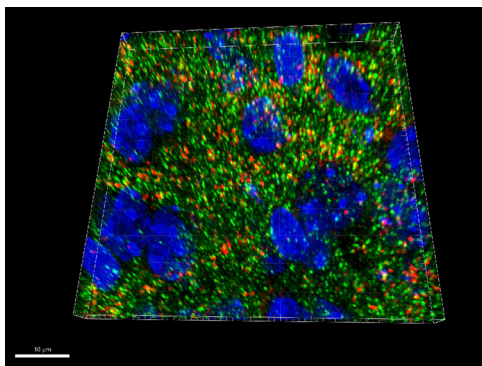
Movie 1. Presynaptic protein VGLUT2 (red), postsynaptic protein HOMER1 (green), and synaptic connection (i.e., double labeled in yellow) in vehicle-treated WT, cortical Layer IV (scale bar: 10 μm). [View online]
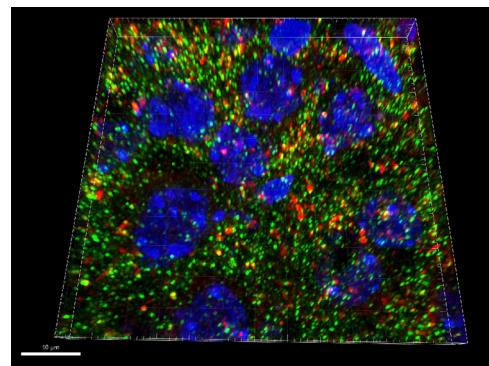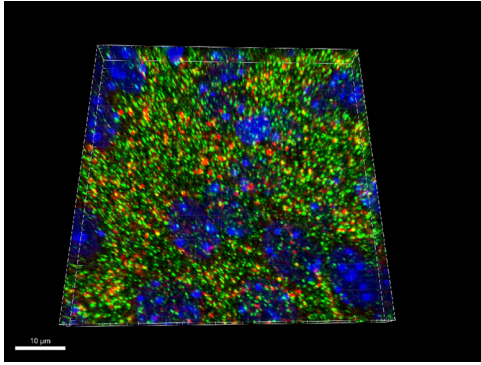

Movie 2. Presynaptic protein VGLUT2 (red), postsynaptic protein HOMER1 (green), and synaptic connection (i.e., double labeled in yellow) in vehicle-treated *prh*, cortical Layer IV (scale bar: 10 μm). [View online]

0.0001 bin-*prh* vs veh-*prh*; Fig. 7*B*, right; see also Movie 2 (veh-*prh*) vs Movie 4 (bin-*prh*) from Layer IV]. Despite the significant improvement in mature synapse numbers (i.e., VGLUT2/HOMER1 double staining) after bindarit treatment, the slight improvements in VGLUT2-only ($p = 0.2830$, bin-*prh* vs veh-*prh* in Layer II/III, $p = 0.1391$, bin-*prh* vs veh-*prh* in Layer IV) or HOMER1-only ($p = 0.1531$, bin-*prh* vs veh-*prh* in Layer II/III, $p = 0.0803$, bin-*prh* vs veh-*prh* in Layer IV) staining did not reach statistical significance (Fig. 7*A*,*B*, left and middle). These findings indicate that neonatal hydrocephalus leads to the impairment of synaptic maturation, and that the anti-inflammatory agent bindarit improves it via controlling myeloid cells functions in the neonatal hydrocephalic brain.

Interneuron morphology is less mature in *prh* cortex and is improved by bindarit treatment

One common complication of neonatal hydrocephalus patients is epilepsy (Vinchon et al., 2012). Epilepsy generally occurs when the balance of neuronal excitation and inhibitory counteraction is perturbed (Treiman, 2001), and thus various agonists of GABA, one of the main inhibitory neurotransmitters, have been prescribed as antiepileptic drugs (Macdonald and Kelly, 1995). As the postnatal cortical Layers II–V were affected and thinner in the *prh* mutant (Fig. 5), we next asked whether GABAergic interneurons, which compose around 20–30% of neocortical neurons in rodents (Markram et al., 2004), are altered in *prh* hydrocephalus mice. DLX5 is a transcription factor that regulates the migration and differentiation of parvalbumin-expressing cortical interneurons (Wang et al., 2010; Lim et al., 2018). Using

Movie 3. Presynaptic protein VGLUT2 (red), postsynaptic protein HOMER1 (green), and synaptic connection (i.e., double labeled in yellow) in bindarit-treated WT, cortical Layer IV (scale bar: 10 μm). [View online]
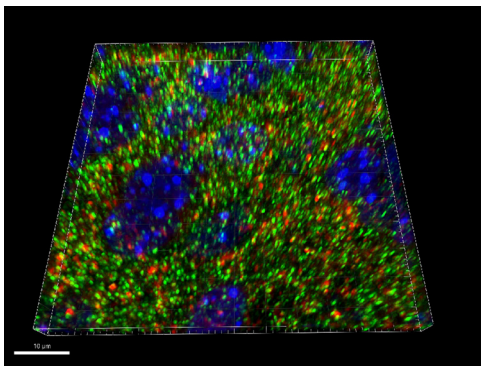
Movie 4. Presynaptic protein VGLUT2 (red), postsynaptic protein HOMER1 (green), and synaptic connection (i.e., double labeled in yellow) in bindarit-treated *prh*, cortical Layer IV (scale bar: 10 μm). [View online]

a DLX5 antibody (Lindtner et al., 2019), we observed a heterogeneous distribution of DLX5$^+$ interneurons but found no difference in the number of positive cells within the cerebral cortex among all groups regardless of genotype or drug treatment ($p = 0.8699$ for genotype, $p = 0.1445$ for drug, $n = 4$ in each group; Fig. 8A). Then we also evaluated non-DLX5-parvalbumin interneurons, such as Calretinin (CALR)-expressing and Calbindin-28 kDa (CALB)-expressing interneurons (Lim et al., 2018). The majority of CALR$^+$ cells in WT were observed in Layer II/III as vertical fusiform cells with long processes traveling perpendicular to the pial surface (Fig. 8B, insets, arrows), as previously reported (Park et al., 2002; Raghanti et al., 2010). The density of CALR$^+$ cells was not different among all groups ($p = 0.2427$ for genotype, $p = 0.7971$ for drug, $n = 4$–5 in each group; Fig. 8B), but CALR$^+$ cells in veh-*prh* cortex lacked their fusiform shape and appeared more rounded (†$p = 0.0347$ compared with veh-WT; Fig. 8B, insets, arrows). This morphologic change was significantly improved in bin-*prh* cortex (*$p = 0.0299$ compared with veh-*prh*, $n = 4$–5 in each group; Fig. 8B). CALB$^+$ cells were heterogeneously distributed, but generally two cell types were observed: pyriform cell bodies with short dendrites in Layer II/II and small to large-sized stellate, multipolar cells in Layer V, as previously reported (Fig. 8C, insets, arrows; Park et al., 2002). The density of CALB$^+$ cells in the upper Layer II/III ($p = 0.6125$ for genotype, $p = 0.7088$ for drug) and lower Layer V ($p = 0.3625$ for genotype, $p = 0.4623$ for drug, $n = 4$–5 in each group) were separately evaluated, but neither of them was different among all groups (lower layers shown in Fig. 8C). However, CALB$^+$ cells with any processes in the lower layers (Fig. 8C, insets, arrows)

were reduced in veh-*prh* and bin-*prh* (††$p = 0.0025$, veh-*prh* vs veh-WT, †$p = 0.0380$, bin-*prh* vs veh-WT), and bindarit treatment did not achieve significant recovery ($p = 0.5564$, bin-*prh* vs veh-*prh*, $n = 4$–5 in each group; Fig. 8C). We attempted to evaluate GABAergic inhibitory synapses with presynaptic protein VGAT and postsynaptic protein GPHN in the upper cortical layers; however, both the immunoreactivities were very sparse even in WT at P8 as observed in a previous report (Virtanen et al., 2018), and therefore inhibitory synapses at this early postnatal age were unable to be compared accurately either between *prh* versus WT or with/without drug treatment. These results show that bindarit treatment can partially rescue interneuron maturation (i.e., dendritic development in CALR$^+$ neurons) in the upper cortical layers, potentially by rescuing the homeostatic microglial function.

Bindarit suppresses microglial inflammatory activation and proliferation in the white matter and restores the ramified-shaped residential microglia in the gray matter

We investigated whether these amoeboid-shaped myeloid cells (Fig. 4A,C,D) in the white matter of *prh* mutants mainly originate from microglia, or peripheral monocyte-derived macrophages which infiltrate into the CNS after the injury. We performed *in situ* hybridization for the microglial signature genes *P2ry12* (purinergic receptor P2Y, G-protein-coupled 12) and *Tmem119* (transmembrane protein 119; Hickman et al., 2013; Butovsky et al., 2014; Bennett et al., 2016), as well as the monocyte signature gene *Ccr2* [chemokine (C-C motif) receptor 2], in combination with IBA1 immunohistochemistry. It has been shown that even after the inflammatory transformation of microglia, these signature genes' expression remains expressed at low levels (Jordão et al., 2019). Strikingly, nearly all the IBA1$^+$ amoeboid-shaped cells in the veh-*prh* white matter were positive for *P2ry12* (Fig. 9A, middle row) and *Tmem119* (Fig. 9B, middle row). Slightly decreased *P2ry12* and *Tmem119* expression in these cells compared with that of ramified-shaped mature microglia in veh-WT (Fig. 9A, top row, B, top row), suggested that they are activated and transformed microglia with proinflammatory phenotype (Jordão et al., 2019). In contrast, we did not observe tissue infiltrating *Ccr2*$^+$ monocytes in the *prh* mutant brain parenchyma at all, and no *Ccr2* expression was detected in these activated IBA1$^+$ cells in the white matter (Fig. 9A, middle row). We confirmed that reliable *Ccr2* signal was observed in monocytes in the blood and some of the IBA1$^+$ *P2ry12*-negative macrophages localized in the subarachnoid space and meninges (Fig. 9A, bottom row, arrowhead). Similarly, *Tmem119* was not expressed in meningeal IBA1$^+$ cells (Fig. 9B, bottom row, arrowhead), validating these mRNA probes for the specific labeling of microglia. Quantification from 100 amoeboid-shaped IBA1$^+$ cells in the white matter ($n = 2$–3) showed that 98% and 85% were positive for *P2ry12* and *Tmem119*, respectively, but not *Ccr2* (Fig. 9C). This result indicated that the majority of these amoeboid-shaped myeloid cells originated from microglia.

Microglia undergo maturation during the postnatal period, during which time they acquire their homeostatic ramified morphology. The majority of the microglia migrate to the brain from the yolk sac (~E9.5), or from the fetal liver (~E13.5; Ginhoux et al., 2013), and keep their proliferative status at low levels in the postnatal brain under normal development (Arnoux et al., 2013; Smolders et al., 2019). In veh-*prh*, the amoeboid-shaped IBA1$^+$ cells in the periventricular white matter often expressed cell proliferation marker Ki67, while only few IBA1$^+$ cells expressed Ki67 in WT and bin-*prh* (Fig. 9D). In addition, there were
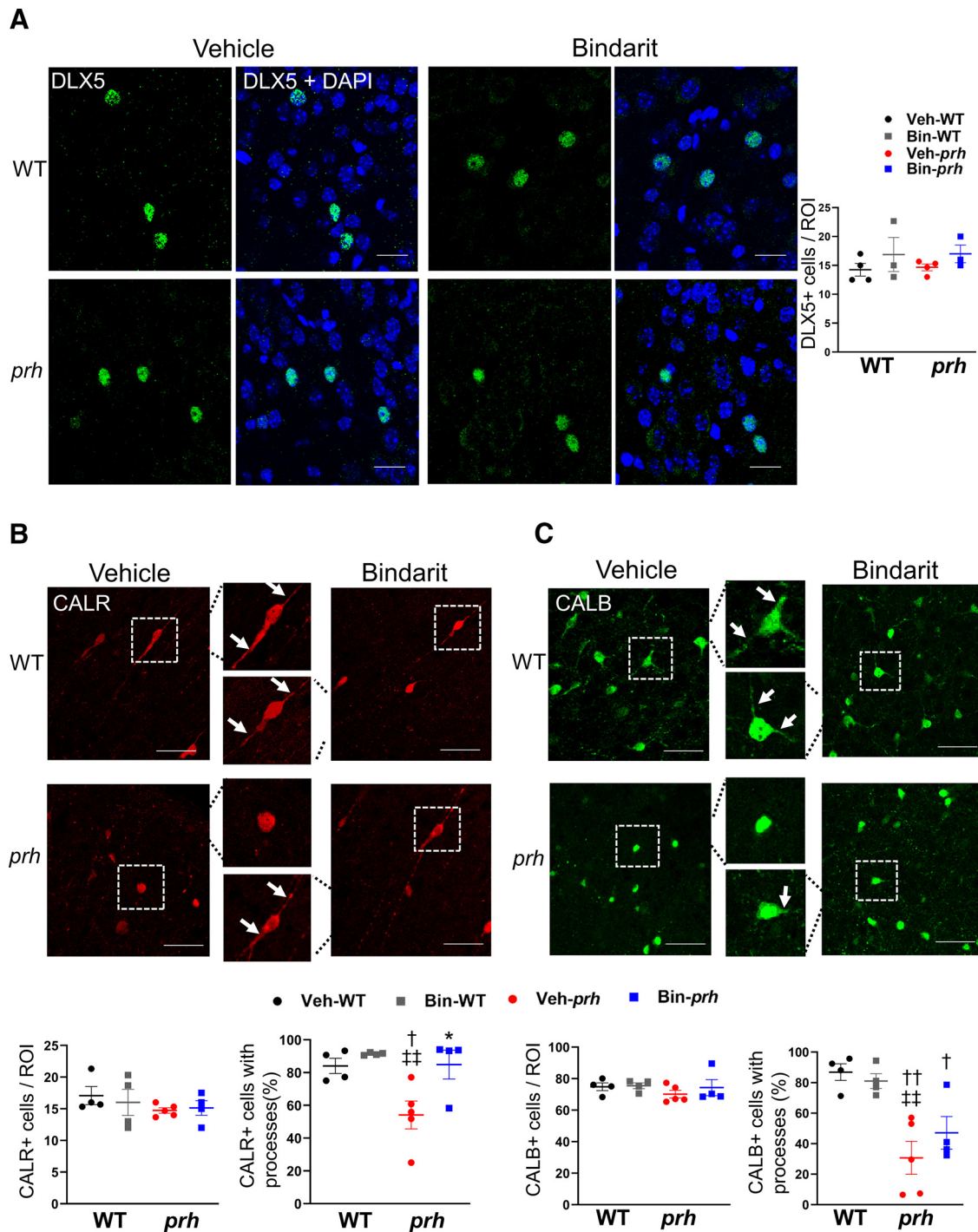
Figure 8. Altered morphology of cortical interneurons in *prh* mutants is partially rescued by bindarit treatment. ***A***, The number of DLX5, a transcriptional factor which regulates parvalbumin-expressing cortical interneuron development, as an average in three ROIs shows no difference in DLX5-expressing interneurons among groups (two-way ANOVA followed by Tukey's test, $n = 4$ in each group; scale bars: 20 μm). ***B***, The number of Calretinin[+] (CALR[+]) interneurons as an average of three ROIs in upper layers is not significantly different among groups (left graph), but the percentages of CALR^{+} cells with processes is significantly reduced in veh-*prh* (†$p = 0.0347$ vs veh-WT, ‡‡$p = 0.0086$ vs bin-WT) and improved in bin-*prh* cortex (*$p = 0.0299$ vs veh-*prh*; right graph; two-way ANOVA followed by Tukey's test, $n = 4$ in each group; scale bars: 50 μm). ***C***, The number of Calbindin D28K[+] (CALB[+]) interneurons as an average of three ROIs in lower layers is not significantly different among groups (left graph), but the percentages of CALB^{+} cells with processes is significantly reduced in veh-*prh* (††$p = 0.0025$ veh-*prh* vs veh-WT, ††$p = 0.0058$ bin-*prh* vs veh-WT, ‡$p = 0.0380$ vs bin-WT) with no significant improvement in bin-*prh* cortex ($p = 0.5564$ vs veh-*prh*; right graph; two-way ANOVA followed by Tukey's test, $n = 4$ in each group; scale bars: 50 μm).

significantly more TUNEL positive IBA1^{+} ramified-shaped microglia in the gray matter of veh-*prh* compared with WT (††$p = 0.0082$ compared with veh-WT; Fig. 9E). Along with this observation, density of ramified-shaped homeostatic microglia in the gray matter was significantly decreased in veh-*prh* compared with WT (†††$p < 0.0006$ compared with veh-WT; Fig. 9F). Interestingly, the number of ramified-shaped microglia in gray matter was significantly restored in bin-*prh* as compared with veh-*prh* (*$p = 0.0140$ compared with veh-*prh*, $n = 6$ in each group; Fig. 9F), with significantly less TUNEL positive cells
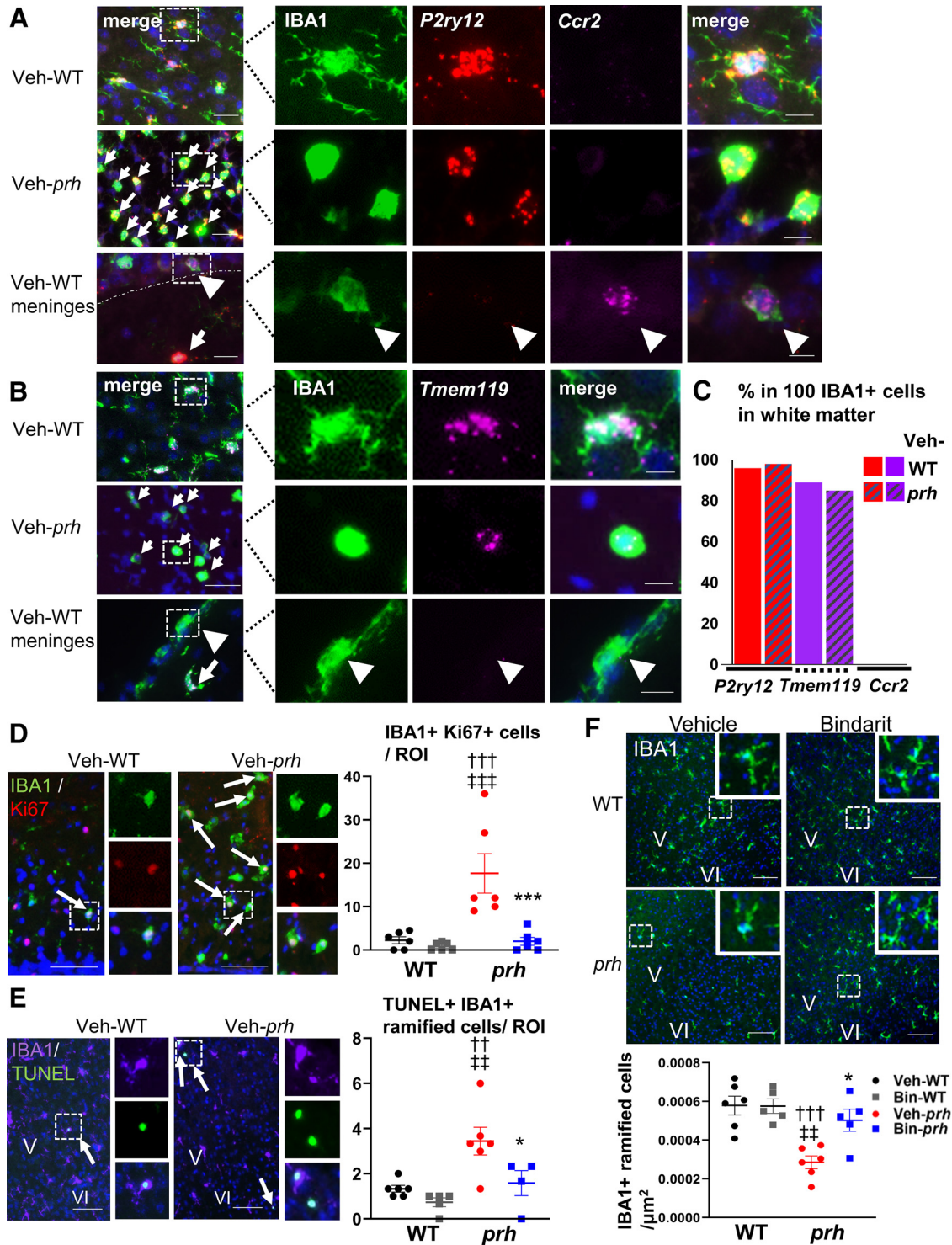
Figure 9. Bindarit suppresses microglial activation in the white matter and restores the ramified microglia in the *prh* gray matter. **A**, The microglial signature gene *P2ry12* (*purinergic receptor P2Y, G-protein-coupled 12*) is expressed on ramified-shaped IBA1$^+$ cells in WTs at P8 (top row). The amoeboid-shaped IBA1$^+$ cells in the white matter (WM) of veh-*prh* at P8 also express *P2ry12* to a lesser extent, but do not express the monocyte signature gene *Ccr2* [chemokine (C-C motif) receptor 2; middle row]. The *Ccr2* probe is validated, and its signal is observed on IBA1$^+$ cells outside the brain in veh-WT at P8, which do not have *P2ry12* signal (bottom row, arrowhead), whereas *P2ry12* is expressed on cortical microglia on the same slide (bottom row, arrow; $n = 3$–4; scale bars: 50 μm for low-magnification pictures, 10 μm for high-magnification pictures). **B**, Another microglial signature gene *Tmem119* is expressed on ramified-shaped IBA1$^+$ cells in veh-WT at P8 (top row). The amoeboid-shaped IBA1$^+$ cells in the WM of veh-*prh* at P8 also express *Tmem119* to a lesser extent (middle row). *Tmem119* is not expressed on IBA1$^+$ cells outside the brain in veh-WT at P8 (bottom row, arrowhead), whereas cortical microglia express *Tmem119* on the same slide (bottom row, arrow; $n = 2$; scale bars: 50 μm for low-magnification pictures, 10 μm for high-magnification pictures). **C**, Graph shows the quantification of *P2ry12* (96%, 98%), *Tmem119* (89%, 85%), and *Ccr2* (0%, 0%) expression in 100 IBA1$^+$ cells ($n = 2$–3) in the WM of veh-WT and veh-*prh*, respectively. All 100 IBA1$^+$ cells quantified in veh-*prh* are amoeboid-shaped cells. **D**, Double-staining of IBA1 and the proliferation marker Ki67 shows very few double labeled cells in the WM of veh-WT (top) but significantly more proliferating amoeboid-shaped IBA1$^+$ cells (arrows) in the WM of veh-*prh* (bottom; †††$p = 0.0009$ vs veh-WT, ‡‡‡$p = 0.0003$ vs bin-WT). This effect is suppressed in bin-*prh* brains (***$p = 0.0008$, two-way ANOVA followed by Tukey's test, $n = 6$ in each group; scale bars: 100 μm). **E**, TUNEL assay with IBA1 staining shows significantly more TUNEL positive (i.e., dying) ramified microglia (arrows) within the gray matter of veh-*prh* cortex (††$p = 0.0082$ vs veh-WT, ‡‡$p = 0.0014$ vs bin-WT). Bindarit treatment significantly reduces this cell death in bin-*prh* cortex (*$p = 0.0411$ vs veh-*prh*; two-way ANOVA followed by Tukey's test, $n = 4$–6 in each group; scale

(*$p = 0.0411$ compared with veh-*prh*, $n = 4$–6 in each group; Fig. 9E). These results suggest that bindarit suppressed proinflammatory activation and proliferation of microglia in the *prh* white matter, while restoring the homeostatic ramified microglia in the developing mutant cortex.

Effect of bindarit on suppressing NF-kB p65 activation in myeloid cells

As bindarit has been reported to specifically downregulate the stimulus-induced inflammatory cytokine expression including *Mcp-1*, via inhibiting NF-kB p65 phosphorylation, subsequent nuclear translocation, and DNA binding (Mora et al., 2012), we performed NF-kB p65 staining to determine its cellular localization. The active nuclear p65 signals were prominent in the IBA1$^+$ amoeboid-shaped cells in veh-*prh* (Fig. 10C), while bin-*prh* showed weak p65 signals mainly in the cytoplasm of the IBA1$^+$ cells to a lesser extent than veh-*prh,* as well as ependymal cells and a fraction of neural progenitor cells in the subventricular zone, SVZ (Fig. 10D), similar to WT (Fig. 10A). The number of p65-expressing IBA1$^+$ cells was significantly reduced in bin-*prh* (Fig. 10E, ****$p < 0.0001$ relative to veh-*prh*). Moreover, the ratio of IBA1$^+$ cells showing nuclear p65 signal was significantly lower in bindarit-treated *prh* cortex ($27.6 \pm 3.2\%$ in veh-*prh* vs $6.1 \pm 10\%$ in bin-*prh*, **$p = 0.0028$; Fig. 10F). In the WT brain, at a homeostatic state, p65 localized in the cytoplasm of ependymal cells (Fig. 10A, short thick arrows), blood vessels (Fig. 10A, arrowhead), and GFAP$^+$ astrocytes with fusiform morphology in the ventricular-subventricular zone (Fig. 10A, left, long arrows, right, clear arrows; Platel and Bordey, 2016). The low level and steady expression of p65 protein in these cell types was in accordance with *Rela* mRNA expression found in the comprehensive mouse brain single-cell RNA sequencing data (http://www.mousebrain.org), validating the specificity of the p65 antibody. Together, these findings indicate that NF-kB signal activation in myeloid cells drives the accumulation of proinflammatory amoeboid-shaped cells and edema formation in the corpus callosum of the neonatal *prh* brain. Importantly, the targeted inhibition of NF-kB activation by bindarit supports a multitude of early postnatal neural cell development processes that are severely affected in the neonatal hydrocephalus and thus may inform an important therapeutic approach for this brain condition.

Bindarit partially improves the swimming locomotor phenotype in *prh* mutants

Motor skills impairment including spasticity and a variable level of paralysis has been identified in pediatric hydrocephalus patients (Rekate, 1999; Pattisapu, 2001). To evaluate the therapeutic significance of the bindarit in early neonatal brain functions, we performed an array of developmental reflex and locomotion tests available in neonatal mice. We performed the surface righting reflex (P4, P6, P8), the grasp reflex (P4, P6, P8), negative geotaxis (P4, P6, P8), and a swim test (P8) in untreated WT ($n = 12$) and *prh* mutants ($n = 18$ for P4 and P6, $n = 15$ for P8). The *prh* mutant showed comparable levels of reflexes tested in the surface righting reflex (Fig. 11A), negative geotaxis test

(Fig. 11B), and the forelimb grasp reflex (data not shown) relative to WT. Both genotypes showed improvement over time in surface righting ($p < 0.0001$) and negative geotaxis ($p = 0.0023$ between P6 and P8; repeated-measures of ANOVA followed by Sidak's test). In contrast, the *prh* mutants showed distinct locomotor phenotypes in the swim test. We found a temporary spastic paraplegia-like phenotype in the water. The spastic phenotype was characterized by either a significant delay when starting hindlimb movements (12 out of 15) or temporary pause during (three out of 15) the sequence of left-right hindlimb alternating movements in the water (7.23 ± 0.79 s for the first trial, and 3.64 ± 0.97 s for the second trial) compared with WT (1.43 ± 0.41 s for first trials and 0.18 ± 0.14 s for second trials) (Fig. 11C, ****$p < 0.0001$ for first trial, *$p = 0.0235$ for second trial, Student's t test; Movies 5 and 6). During this time, the mutants extended hindlimbs with toes spread, which is similar to adult rats exhibiting spasticity phenotypes as a consequence of injury to upper motor neurons (Ryu et al., 2017, 2021) or neonatal V2b-ablated mice with pronounced extension of the hindlimbs and impairment of hindlimb flexion movement in the tail suspension test (Britz et al., 2015). Following this temporary spastic phenotype, *prh* mutants eventually started to move their hindlimbs but showed reduced frequency of alternating hindlimbs relative to WT (Fig. 11D, ****$p < 0.0001$ for first trials, *$p = 0.0127$ for second trials, Student's t test). Both of these phenotypes became less obvious in the second trial, which could be explained by habituation or learning. In fact, in WT, the frequency of alternating hindlimbs becomes slower in second trials than first trials ($p = 0.0030$, Student's t test), probably reflecting habituation or learning in the swim test. Bindarit treatment improved the spastic phenotype in the mutants during the first trial compared with veh-*prh* (Fig. 11E, **$p = 0.0086$, one-way ANOVA followed by *post hoc* Sidak's test) (Movie 7). Frequency of alternating hindlimbs was not reduced in both veh-*prh* and bin-*prh* compared with veh-WT (Fig. 11F), mainly because the frequency was overall reduced in veh-WT relative to untreated WT (Fig. 11D), as daily injection may have affected the baseline behavior in veh-WT. From these results, we showed that *prh* mutant had a locomotor defect in the swim test which resembles mild spasticity and paraplegia phenotypes in nonweight-bearing environments (i.e., swimming) and bindarit partially, but significantly, improved this phenotype.

Discussion

Notwithstanding the common finding of neuroinflammation in pediatric hydrocephalus (Savman et al., 2002; Ulfig et al., 2004; Schmitz et al., 2007; Habiyaremye et al., 2017), the role of inflammation and activated myeloid cells in hydrocephalic brains remains largely unknown. The common histologic changes in neurons in neonatal hydrocephalus, including reduced dendritic arborization and axonal growth, have been considered to be secondary to ventriculomegaly and tissue compression (Del Bigio, 2010; Femi-Akinlosotu et al., 2019). Therefore, the clinical treatment for hydrocephalus has been almost solely focused on CSF diversion (Kahle et al., 2016). Here, we examined myeloid cell activation in a robust neonatal hydrocephalus model and showed that inhibiting neuroinflammation via suppressing NF-kB activation significantly improves neural cell development and motor behavior deficits, despite ongoing ventriculomegaly in these brains.

To examine inflammatory gene expression in the neonatal hydrocephalic brain, we identified a number of upregulated and

←

bars: 100 μm). ***F***, The density of ramified microglia within the gray matter (μm^2) is significantly reduced in veh-*prh* (†††$p = 0.0006$ vs veh-WT, ‡‡$p = 0.0012$ vs bin-WT), and this reduction is significantly restored in bin-*prh* cortex (*$p = 0.0140$ vs veh-*prh*; two-way ANOVA followed by Tukey's test, $n = 6$ in each group; scale bars: 100 μm).
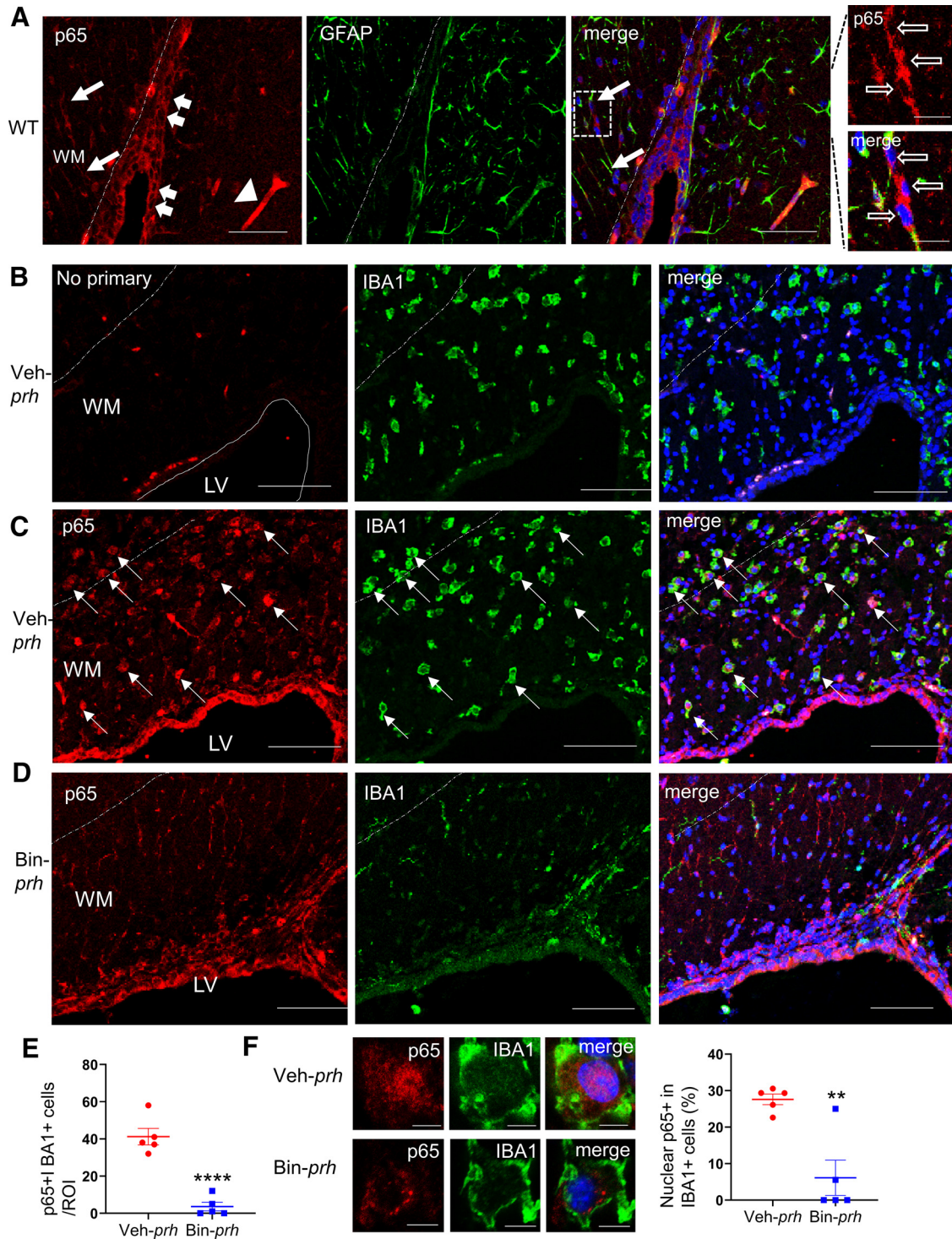
Figure 10. Bindarit works on activated microglia through suppressing NF-kB p65 activation in the white matter. **A**, In P8 WT brains, NF-kB p65 signals are seen in the cytoplasm of ependymal cells (short arrows), vessels (arrowhead), and GFAP$^+$ astrocytes with fusiform morphology in the ventricular-subventricular zone (long arrows; high power, far right, open arrows; scale bars: 50 μm). **B**, In veh-*prh* sections stained with no primary antibody as a control, only red blood cell auto-fluorescence is observed which is easily identified by the morphology and size of the cells (scale bars: 50 μm). **C**, p65 signals in veh-*prh* are seen in IBA1$^+$ amoeboid-shaped cells in the white matter, both within the nucleus and cytoplasm (arrows), along with cytoplasmic signals in the ependymal, vessel, and some radial glial cells (scale bars: 50 μm). **D**, p65 signals in bin-*prh* sections are mainly within cytoplasm of the ependymal and fusiform-shaped astrocytic cells as in WT brain, or to a lesser extent in IBA1$^+$ cells than that in veh-*prh* (scale bars: 50 μm). **E**, The total number of p65-expressing IBA1$^+$ cells per three ROIs per animal is significantly reduced in bin-*prh* cortex (****$p < 0.0001$ relative to veh-*prh*, Student's t test, $n = 5$). **F**, The percentage of p65 nuclear expression (shown as veh-*prh*) rather than cytoplasmic expression (bin-*prh*) in all p65-expressing IBA1$^+$ cells is 27.6 $\pm$ 3.2% in veh-*prh*, and this is significantly reduced (6.1 $\pm$ 10%) in bin-*prh* cortex (**$p = 0.0028$ relative to veh-*prh*, Student's t test, $n = 5$ in each group, total >200 p65$^+$ cells; scale bars: 5 μm).

downregulated genes, which represented microglia/macrophage activation, NF-kB activation, and specific cytokine upregulation (e.g., *Mcp-1*, *Tnfa*, *Ccl3*) in *prh* mutants. We demonstrated that bindarit, a potent anti-inflammatory drug that suppresses microglia/macrophage activation via NF-kB pathways (Mora et al., 2012; Oddi et al., 2019), significantly reduced proinflammatory cytokine production, including *Mcp-1* in amoeboid-shaped IBA1$^+$ cells in the *prh* brain. Furthermore, this treatment
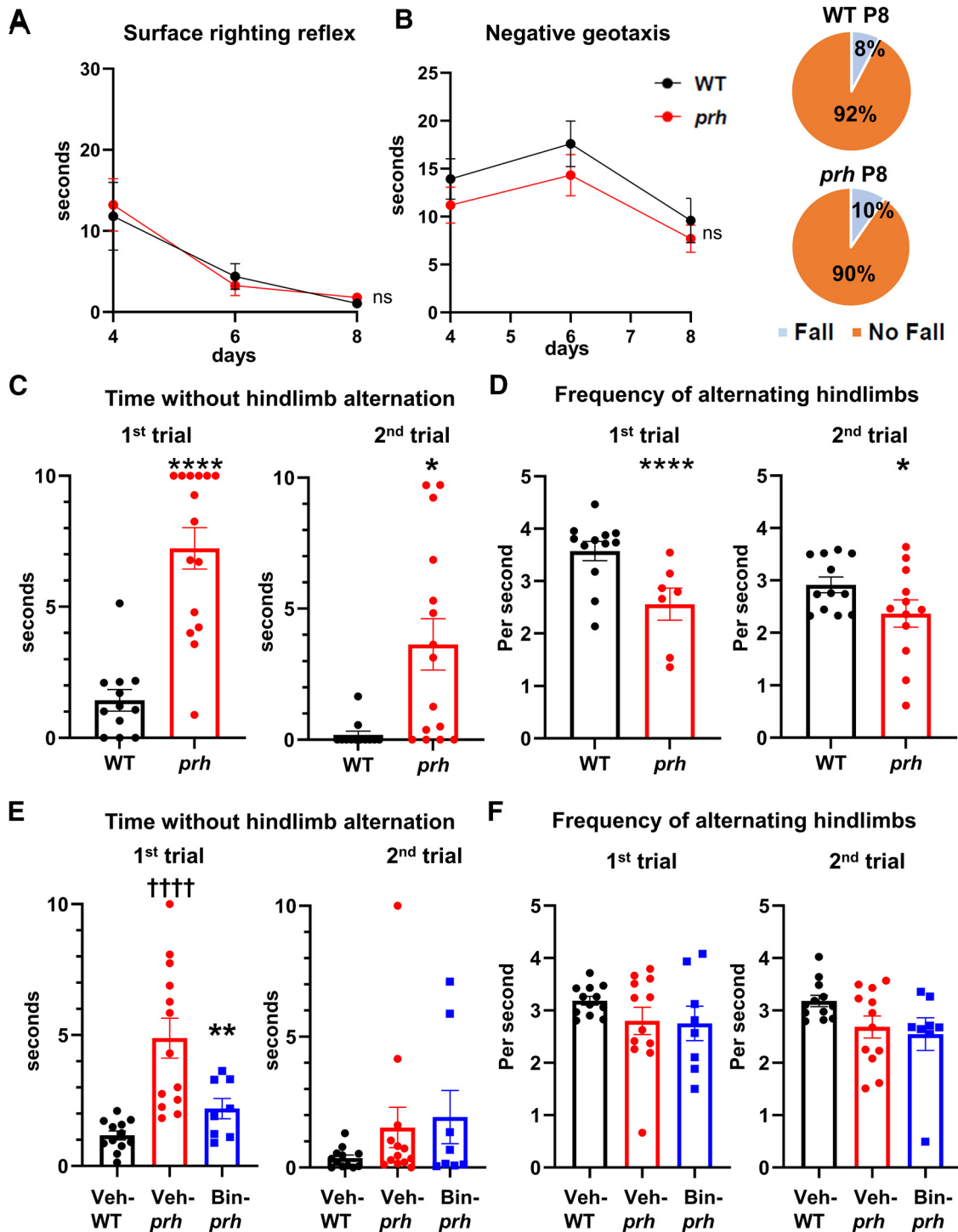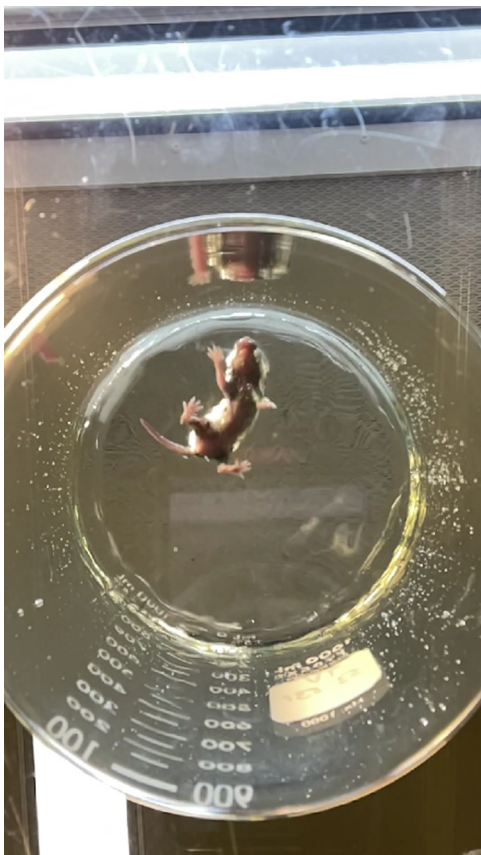
Figure 11. Bindarit partially improves the swimming locomotor phenotype in *prh* mutants. ***A***, Both untreated WT and *prh* show improvement in surface righting reflex over time (****$p < 0.0001$) and there is no difference between WT and *prh* ($p = 0.8627$; $n = 12–18$ in each group, repeated measures ANOVA, followed by *post hoc* Sidak's test). ***B***, There is no difference in the time for negative geotaxis between untreated WT and *prh* ($p = 0.1914$) and both genotypes have significant improvement over time between P6 and P8 ($p = 0.0023$; $n = 12–18$ in each group, repeated measures ANOVA, followed by *post hoc* Sidak's test). The frequency of falling from the surface during the negative geotaxis test is similar in WT (8%) and *prh* mutants (10%). ***C***, During swim testing, untreated *prh* show significantly longer "time without hindlimb alternation" or spastic time, relative to WT, both in first trials and second trials on putting *prh* into the warm water (****$p < 0.0001$ for first trial, *$p = 0.0235$ for second trial, $n = 12–15$ in each group, Student's *t* test). ***D***, Frequency of alternating hindlimbs is significantly less in *prh* relative to WT (****$p < 0.0001$ for first trial, *$p = 0.0127$ for second trial, Student's *t* test). ***E***, Vehicle-treated (veh-)*prh* show significantly longer time without hindlimb alternation, relative to veh-WT (††††$p < 0.0001$), and bindarit treatment significantly improved and shortened this spastic time compared with veh-*prh*, in the first trials (**$p = 0.0086$, one-way ANOVA followed by *post hoc* Sidak's test, $n = 8–13$ in each group), but there is no significant difference among the groups in the second trials ($p = 0.2647$, one-way ANOVA). ***F***, There is no difference among veh-WT, veh-*prh*, and bin-*prh* in the frequency of alternating hindlimbs, excluding the time without hindlimb alternation, in the first ($p = 0.3339$) or second trials ($p = 0.0861$; $n = 8–13$ in each group, one-way ANOVA).

Movie 5. Swim test in untreated WT (first trial). [View online]
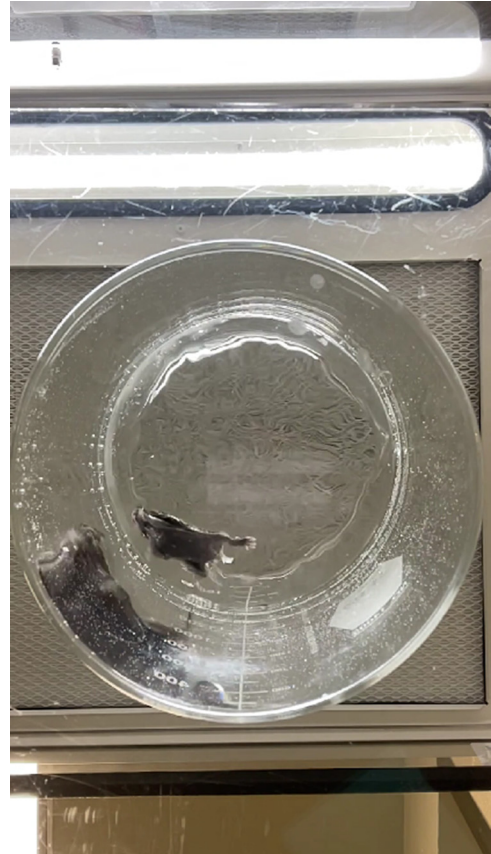
Movie 7. Swim test in bindarit-treated *prh* (first trial). [View online]

reduced edema formation in the periventricular white matter of the hydrocephalic *prh* brain. The activated myeloid cells observed in the *prh* periventricular white matter at P8 were actively proliferating and we propose that they are most likely microglia in origin, based on our findings in microglia-specific gene expression and the absence of parenchymal infiltrating monocytes in this model (Fig. 9A–C). Our results suggest that microglia in neonatal hydrocephalic brains use the NF-kB/MCP-1 pathway to transform from homeostatic/ramified states to proinflammatory/amoeboid states, which has been observed in other neuronal insult models (Hanisch and Kettenmann, 2007; Graeber and Streit, 2010). These cells acquire expression of immature microglial gene signatures (Moyon et al., 2015) and become more proliferative and migratory, with the production of proinflammatory cytokines (Kaur et al., 2007). Although the direct upstream cellular events of NF-kB/MCP-1 activation in hydrocephalus remain unclear, we showed therapeutic potential of NF-kB p65 inhibition in attenuating the subsequent proinflammatory responses caused by a broad range of damage-associated molecular patterns (DAMPs) signals and their receptors including TLR4.

Bindarit is a small-molecule drug available both orally and by subcutaneous/intravenous/intraperitoneal injection and has shown its benefits in the CNS disease models (Cerri et al., 2016). We showed that subcutaneously-injected bindarit reaches the brain at physiologically effective ($>50 \ \mu$M) levels (Fig. 2A–C). Recent work showed that bindarit binds to Fatty acid-binding protein (FABP)4 to exert its NF-kB modulating effect (Oddi et al., 2019), and thus FABP4 (Duffy et al., 2017) in microglia could be the target of bindarit. Possible effects and mechanism of bindarit on other cell types remain for future investigation.

Movie 6. Swim test in untreated *prh* (first trial). [View online]

Our findings of targeting microglia align with some previous findings in doxycycline-analog, minocycline treatment for kaolin-induced hydrocephalus models (McAllister and Miller, 2010) and other neonatal brain injuries (Dommergues et al., 2003; Fox et al., 2005). Currently, minocycline is not recommended for treating children especially with hydrocephalus because of its possible side effects of raising intracranial pressure. On the other hand, specific modulation of the TLR4/NF-kB signaling in hydrocephalus may be more beneficial as it also may decrease CSF overproduction in the choroid plexus and blood-brain barrier breakdown reported in other neonatal brain injury models (Karimy et al., 2017, 2020a,b). Blocking TLR4/NF-kB signaling prevents posthemorrhagic vasospasm and platelet-derived IL-6 release and neutrophil invasion (Karimy et al., 2020b). While taking advantage of a broad function of bindarit in NF-kB modulation (Mora et al., 2012; Oddi et al., 2019), our study demonstrated that blocking a proinflammatory response is beneficial for neural cell development in pediatric hydrocephalus. Higher levels of MCP-1 protein have been noted in the CSF of hydrocephalus patients (Killer et al., 2010), and *Mcp-1* mRNA in *prh* brains directly correlated with the severity of ventriculomegaly in this model. *Mcp-1* is a well-known downstream target of the TLR4/NF-kB pathway and a mediator of the microglia/monocyte responses (Platten et al., 2003; Deng et al., 2009). Therefore, MCP-1 may become a good biomarker to monitor neuroinflammation levels in hydrocephalus patients.

One of the most drastic neuroprotective effects of bindarit in neonatal hydrocephalus was the preservation of cortical Layer II–IV thickness, independent of ventricular size restoration. Similar to previous findings in other hydrocephalus models (Del Bigio and Zhang, 1998), we found no apoptotic neurons nor astrocytes. Importantly, however, our data showed that gray matter microglia undergo apoptotic cell death, further validating the loss of homeostatic microglia in perinatal hydrocephalus. The mouse cortex completes neuronal cell migration around P4 and proceeds to elaborate dendrites and synapse formation during the first three postnatal weeks (Innocenti and Price, 2005; Kast and Levitt, 2019). Microglia in the postnatal brain play a vital role in regulating brain development through supporting axon guidance, myelination, synaptic patterning, and neurogenesis (Schafer and Stevens, 2015; Mosser et al., 2017; Lenz and Nelson, 2018; Rosin et al., 2018; Cserép et al., 2021). Therefore, the observed microglial dysfunction in *prh* hydrocephalic brains likely affects cortical neuronal maturation and synaptogenesis. Indeed, we found that the number of mature excitatory synapses, double stained with presynaptic VGLUT2 and postsynaptic HOMER1 markers, were severely reduced in veh-*prh*. Nevertheless, it was significantly recovered by bindarit treatment along with the restoration of homeostatic microglia. This result suggests that bindarit treatment improved synaptogenesis by preserving the function of ramified-shaped microglia, as proposed in adult Layer II/III neurons (Akiyoshi et al., 2018). The effects of bindarit on enhancing GABAergic interneuron maturation in CALR$^+$ interneurons also suggest the necessity of microglial physiological function on the development of inhibitory neurons and cortical networks (Favuzzi et al., 2021), as seen in the microglia-depleted embryonic brain (Squarzoni et al., 2014). As we observe no detrimental effect of bindarit in the developing WT brains, we propose that the proinflammatory microglia-targeting therapy (e.g., bindarit) may be more beneficial for brain development than removal of all microglia (e.g., using colony-stimulating factor-1 receptor inhibitor) to alleviate neuroinflammation and promote healthy brain development.

Similarly, we noticed that white matter is significantly injured with reduced myelination and less vascular densities in *prh* brains. Accordingly, periventricular white matter injury and myelination delay has been described in neonatal hydrocephalus patients (Gadsdon et al., 1979; Hanlo et al., 1997) and rodent models (Del Bigio et al., 1997; Khan et al., 2006). Two lines of evidence that microglia play essential roles in oligodendrocyte regulation and myelination are: (1) microglial ablation leads to a reduced number of oligodendrocyte precursor cells (OPCs; Hagemeyer et al., 2017), and (2) inflammatory microglia aggressively phagocytose OPCs in the white matter of *Cnp* knock-outs (Garcia-Agudo et al., 2019). It is noteworthy that bindarit-treated hydrocephalus restored the number of resident microglia, which may have contributed to the improved myelination observed.

Lastly, our novel finding of locomotor defects in the swim test using *prh* mice suggests a hydrocephalus-related spasticity. Interestingly, previous reports using a rat model of spinal cord injury that quantitatively evaluated "spasticity" found similar postural findings in a swim test (Ryu et al., 2017, 2021). Spasticity has been reported in pediatric hydrocephalus populations (Pattisapu, 2001). Theoretically, any injury to, or delay in development of the descending innervation from cortex to spinal motor neuron, including corticospinal tract (CST) and corticoreticular input to the medulla, or potentially the ascending innervations, can cause spasticity (Wieters et al., 2021). The CST develops by around P8 in mice (Gianino et al., 1999; Namikawa et al., 2015). Spinothalamic and thalamocortical pathways, which carry ascending sensory information and can also affect motor function, develop embryonically (Fitzgerald, 2005; Davidson et al., 2010). We also noted that the frequency of alternating hindlimbs in *prh* was mildly reduced, likely indicating their reduced motor function in the no-weight-environment in addition to spasticity. Bindarit significantly shortened the spastic time in water, which suggests that reducing inflammatory damage improved the development of motor circuits, though further investigation is needed. The negative findings of general developmental reflexes in *prh* could be because of their compensatory mechanism in intracranial pressure with abnormally enlarged cranial volume (Fig. 2H; Abdelhamed et al., 2018), as suggested in some forms of human neonatal hydrocephalus (Amiel-Tison et al., 2002; Kiesler and Ricer, 2003).

In the current study, we demonstrate that activated myeloid cells contribute to altered cortical development in *prh* mutant brains and that suppression of this neuroinflammation with bindarit ameliorates microglial, neuronal, and behavioral alterations in this mouse genetic model of neonatal hydrocephalus. In our continued efforts to achieve better neurologic outcomes in neonatal hydrocephalus patients, this study provides molecular insights and potential translatable therapeutic targets, which may redefine the standard care for this condition. The limitation of this study is that *prh* mutants die at a young age (Abdelhamed et al., 2018), and thus, we could not observe the long-term effect of bindarit treatment. Nevertheless, our findings suggest that modulation of neuroinflammation, in combination with CSF diversion surgery, may provide a significant improvement for treatment of pediatric hydrocephalus.

References

Abdelaziz MH, Abdelwahab SF, Wan J, Cai W, Huixuan W, Jianjun C, Kumar KD, Vasudevan A, Sadek A, Su Z, Wang S, Xu H (2020) Alternatively activated macrophages; a double-edged sword in allergic asthma. J Transl Med 18:58.

Abdelhamed Z, Vuong SM, Hill L, Shula C, Timms A, Beier D, Campbell K, Mangano FT, Stottmann RW, Goto J (2018) A mutation in Ccdc39 causes neonatal hydrocephalus with abnormal motile cilia development in mice. Development 145:dev154500.

Abdi K, Lai CH, Paez-Gonzalez P, Lay M, Pyun J, Kuo CT (2018) Uncovering inherent cellular plasticity of multiciliated ependyma leading tot ventricular wall transformation and hydrocephalus. Nat Commun 9:1655.

Adencreutz M, Hau J (2008) Gender and cognitive aspects of neonatal and juvenile neuromuscular locomotor development of F1 hybrid mice in swim tests. Lab Anim 42:26–33.

Akiyoshi R, Wake H, Kato D, Horiuchi H, Ono R, Ikegami A, Haruwaka K, Omori T, Tachibana Y, Moorhouse AJ, Nabekura J (2018) Microglia enhance synapse activity to promote local network synchronization. eNeuro 5:ENEURO.0088-18.2018.

Amiel-Tison C, Gosselin J, Infante-Rivard C (2002) Head growth and cranial assessment at neurological examination in infancy. Dev Med Child Neurol 44:643–648.

Arnoux I, Hoshiko M, Mandavy L, Avignone E, Yamamoto N, Audinat E (2013) Adaptive phenotype of microglial cells during the normal postnatal development of the somatosensory "Barrel" cortex. Glia 61:1582–1594.

Ayannuga OA, Shokunbi MT, Naicker TA (2016) Myelin sheath injury in kaolin-induced hydrocephalus: a light and electron microscopy study. Pediatr Neurosurg 51:61–68.

Badano JL, Mitsuma N, Beales PL, Katsanis N (2006) The ciliopathies: an emerging class of human genetic disorders. Annu Rev Genomics Hum Genet 7:125–148.

Bennett ML, Bennett FC, Liddelow SA, Ajami B, Zamanian JL, Fernhoff NB, Mulinyawe SB, Bohlen CJ, Adil A, Tucker A, Weissman IL, Chang EF, Li G, Grant GA, Hayden Gephart MG, Barres BA (2016) New tools for studying microglia in the mouse and human CNS. Proc Natl Acad Sci USA 113:E1738–E1746.

Bercury KK, Macklin WB (2015) Dynamics and mechanisms of CNS myelination. Dev Cell 32:447–458.

Bhatia M, Ramnath RD, Chevali L, Guglielmotti A (2005) Treatment with bindarit, a blocker of MCP-1 synthesis, protects mice against acute pancreatitis. Am J Physiol Gastrointest Liver Physiol 288:G1259–G1265.

Boer K, Spliet WGM, van Rijen PC, Redeker S, Troost D, Aronica E (2006) Evidence of activated microglia in focal cortical dysplasia. J Neuroimmunol 173:188–195.

Botfield H, Gonzalez AM, Abdullah O, Skjolding AD, Berry M, McAllister JP, Logan A (2013) Decorin prevents the development of juvenile communicating hydrocephalus. Brain 136:2842–2858.

Bouyssi-Kobar M, Du Plessis AJ, McCarter R, Brossard-Racine M, Murnick J, Tinkleman L, Robertson RL, Limperopoulos C (2016) Third trimester brain growth in preterm infants compared with in utero healthy fetuses. Pediatrics 138:e20161640.

Britz O, Zhang J, Grossman KS, Dyck J, Kim JC, Dymecki S, Gosgnach S, Goulding M (2015) A genetically defined asymmetry underlies the inhibitory control of flexor-extensor locomotor movements. Elife 4:e04718.

Butovsky O, Jedrychowski MP, Moore CS, Cialic R, Lanser AJ, Gabriely G, Koeglsperger T, Dake B, Wu PM, Doykan CE, Fanek Z, Liu L, Chen Z, Rothstein JD, Ransohoff RM, Gygi SP, Antel JP, Weiner HL (2014) Identification of a unique TGF-β-dependent molecular and functional signature in microglia. Nat Neurosci 17:131–143.

Cerri C, Genovesi S, Allegra M, Pistillo F, Püntener U, Guglielmotti A, Perry VH, Bozzi Y, Caleo M (2016) The chemokine CCL2 mediates the seizure-enhancing effects of systemic inflammation. J Neurosci 36:3777–3788.

Cherry JD, Olschowka JA, O'Banion MK (2014) Neuroinflammation and M2 microglia: the good, the ad, and the inflamed. J Neuroinflammation 11:98.

Cserép C, Pósfai B, Dénes Á (2021) Shaping neuronal fate: functional heterogeneity of direct microglia-neuron interactions. Neuron 109:222–240.

Cui Y, Zheng Y, Liu X, Yan L, Fan X, Yong J, Hu Y, Dong J, Li Q, Wu X, Gao S, Li J, Wen L, Qiao J, Tang F (2019) Single-cell transcriptome analysis maps the developmental track of the human heart. Cell Rep 26:1934–1950.

Davidson S, Truong H, Giesler GJ Jr (2010) Quantitative analysis of spinothalamic tract neurons in adult and developing mouse. J Comp Neurol 518:3193–3204.

Del Bigio MR (2001) Myelin sheath injury in kaolin-induced hydrocephalus: a light and electron microscopy study. Neurosurg Clin N Am 12:639–649.

Del Bigio MR (2010) Neuropathology and structural changes in hydrocephalus. Dev Disabil Res Revs 16:16–22.

Del Bigio MR, Di Curzio DL (2016) Nonsurgical therapy for hydrocephalus: a comprehensive and critical review. Fluids Barriers CNS 13:3.

Del Bigio MR, Zhang YW (1998) Cell death, axonal damage, and cell birth in the immature rat brain following induction of hydrocephalus. Exp Neurol 154:157–169.

Del Bigio MR, da Silva MC, Drake JM, Tuor UI (1994) Acute and chronic cerebral white matter damage in neonatal hydrocephalus. Can J Neurol Sci 21:299–305.

Del Bigio MR, Kanfer JN, Zhang YW (1997) Myelination delay in the cerebral white matter of immature rats with kaolin-induced hydrocephalus is reversible. J Neuropathol Exp Neurol 56:1053–1066.

Deng YY, Lu J, Ling EA, Kaur C (2009) Monocyte chemoattractant protein-1 (MCP-1) produced via NF-κB signaling pathway mediates migration of amoeboid microglia in the periventricular white matter in hypoxic neonatal rats. Glia 57:604–621.

Deren KE, Packer M, Forsyth J, Milash B, Abdullah OM, Hsu EW, McAllister JP (2010) Reactive astrocytosis, microgliosis and inflammation in rats with neonatal hydrocephalus. Exp Neurol 226:110–119.

Dominguez-Pinos MD, Paez P, Jimenez AJ, Weil B, Arraez MA, Perez-Figares JM, Rodringuez EM (2005) Ependymal denudation and alterations of the subventricular zone occur in human fetuses with a moderate communicating hydrocephalus. J Neuropathol Exp Neurol 64:595–604.

Dommergues MA, Plaisant F, Verney C, Gressens P (2003) Early microglial activation following neonatal excitotoxic brain damage in mice: a potential target for neuroprotection. Neuroscience 121:619–628.

Duffy CM, Xu H, Nixon JP, Bernlohr DA, Butterick TA (2017) Identification of a fatty acid-binding protein4-UCP2 axis regulating microglial mediated neuroinflammation. Mol Cell Neurosci 80:52–57.

Emmert AS, Iwasawa E, Shula C, Schultz P, Lindquist D, S Dunn R, Fugate EM, Hu YC, Mangano FT, Goto J (2019) Impaired neural differentiation and glymphatic CSF flow in the Ccdc39 rat model of neonatal hydrocephalus: genetic interaction with L1cam. Dis Model Mech 12:dmm040972.

Fabregat A, Sidiropoulos K, Garapati P, Gillespie M, Hausmann K, Haw R, Jassal B, Jupe S, Korninger F, McKay S, Matthews L, May B, Milacic M, Rothfels K, Shamovsky V, Webber M, Weiser J, Williams M, Wu G, Stein L, et al. (2016) The reactome pathway knowledgebase. Nucleic Acids Res 44:D481–D487.

Fame RM, MacDonald JL, Macklis JD (2011) Development, specification, and diversity of callosal projection neurons. Trends Neurosci 34:41–50.

Fan X, Dong J, Zhong S, Wei Y, Wu Q, Yan L, Yong J, Sun L, Wang X, Zhao Y, Wang W, Yan J, Wang X, Qiao J, Tang F (2018) Spatial transcriptomic survey of human embryonic cerebral cortex by single-cell RNA-seq analysis. Cell Res 28:730–745.

Favuzzi E, Huang S, Saldi GA, Binan L, Ibrahim LA, Fernández-Otero M, Cao Y, Zeine A, Sefah A, Zheng K, Xu Q, Khlestova E, Farhi SL, Bonneau R, Datta SR, Stevens B, Fishell G (2021) GABA-receptive microglia selectively sculpt developing inhibitory circuits. Cell 184:4048–4063.

Feather-Schussler DN, Ferguson TS (2016) A battery of motor tests in a neonatal mouse model of cerebral palsy. J Vis Exp 117:53569.

Feldner A, Adam MG, Tetzlaff F, Moll I, Komljenovic D, Sahm F, Bäuerle T, Ishikawa H, Schroten H, Korff T, Hofmann I, Wolburg H, Deimling A, Fischer A (2017) Loss of Mpdz impairs ependymal cell integrity leading to perinatal-onset hydrocephalus in mice. EMBO Mol Med 9:890–905.

Femi-Akinlosotu OM, Shokunbi MT, Naicker T (2019) Dendritic and synaptic degeneration in pyramidal neurons of the sensorimotor cortex in neonatal mice with kaolin-induced hydrocephalus. Front Neuroanat 13:38.

Fitzgerald M (2005) The development of nociceptive circuits. Nat Rev Neurosci 6:507–520.

Fox C, Dingman A, Derugin N, Wendland MF, Manabat C, Ji S, Ferriero DM, Vexler ZS (2005) Minocycline confers early but transient protection in the immature brain following focal cerebral ischemia-reperfusion. J Cereb Blood Flow Metab 25:1138–1149.

Fujiyama F, Furuta T, Kaneko T (2001) Immunocytochemical localization of candidates for vesicular glutamate transporters in the rat cerebral cortex. J Comp Neurol 435:379–387.

Furey CG, Choi J, Jin SC, Zeng X, Timberlake AT, Nelson-Williams C, Mansuri MS, Lu Q, Duran D, Panchagnula S, Allocco A, Karimy JK,

Khanna A, Gaillard JR, DeSpenza T, Antwi P, Loring E, Butler WE, Smith ER, Warf BC, et al. (2018) De novo mutation in genes regulating neural stem cell fate in human congenital hydrocephalus. Neuron 99:302–314.

Gadsdon D, Variend S, Emery J (1979) Myelination of the corpus callosum. II. The effect of relief of hydrocephalus upon the processes of myelination. Z Kinderchir Grenzgeb 28:314–321.

Garcia-Agudo LF, Janova H, Sendler LE, Arinrad S, Steixner AA, Hassouna I, Balmuth E, Ronnenberg A, Schopf N, Flier FJ, Begemann M, Martens H, Weber MS, Boretius S, Nave KA, Ehrenreich AH (2019) Genetically induced brain inflammation by Cnp deletion transiently benefits from microglia depletion. FASEB J 33:8634–8647.

Gasque P, Singhrao S, JW N, Wang P, Sayah S, Fontaine M, Morgan B (1998) The receptor for complement anaphylatoxin C3a is expressed by myeloid cells and nonmyeloid cells in inflamed human central nervous system: analysis in multiple sclerosis and bacterial meningitis. J Immunol 160:3543–3554.

Ge S, Shrestha B, Paul D, Keating C, Cone R, Guglielmotti A, Pachter JS (2012) The CCL2 synthesis inhibitor bindarit targets cells of the neurovascular unit, and suppresses experimental autoimmune encephalomyelitis. J Neuroinflammation 9:171.

Gianino S, Stein SA, Li H, Lu X, Biesiada E, Ulas J, Xu XM (1999) Postnatal growth of corticospinal axons in the spinal cord of developing mice. Brain Res Dev Brain Res 112:189–204.

Ginhoux F, Lim S, Hoeffel G, Low D, Huber T (2013) Origin and differentiation of microglia. Front Cell Neurosci 7:45.

Goulding DS, C Vogel R, Pandya CD, Shula C, Gensel JC, Mangano FT, Goto J, Miller BA (2020) Neonatal hydrocephalus leads to white matter neuroinflammation and injury in the corpus callosum of Ccdc39 hydrocephalic mice. J Neurosurg Pediatr 25:476–483.

Graeber MB, Streit WJ (2010) Microglia: biology and pathology. Acta Neuropathol 119:89–105.

Gutierrez-Mecinas M, Kuehn ED, Abraira VE, Polgár E, Watanabe M, Todd AJ (2016) Immunostaining for Homer reveals the majority of excitatory synapses in laminae I-III of the mouse spinal dorsal horn. Neuroscience 329:171–181.

Habiyaremye G, Morales DM, Morgan CD, McAllister JP, CreveCoeur TS, Han RH, Gabir M, Baksh B, Mercer D, Limbrick DD Jr (2017) Chemokine and cytokine levels in the lumbar cerebrospinal fluid of preterm infants with post-hemorrhagic hydrocephalus. Fluids Barriers CNS 14:35.

Hagemeyer N, Hanft KM, Akriditou MA, Unger N, Park ES, Stanley ER, Staszewski O, Dimou L, Prinz M (2017) Microglia contribute to normal myelinogenesis and to oligodendrocyte progenitor maintenance during adulthood. Acta Neuropathol 134:441–458.

Hanisch UK, Kettenmann H (2007) Microglia: active sensor and versatile effector cells in the normal and pathologic brain. Nat Neurosci 10:1387–1394.

Hanlo PW, Gooskens RJHM, van Schooneveld M, Tulleken CAF, van der Knaap MS, Faber JAJ, Willemse J (1997) The effect of intracranial pressure on myelination and the relationship with neurodevelopment in infantile hydrocephalus. Dev Med Child Neurol 39:286–291.

Harris NG, McAllister II JP, Conaughty JM, Jones HC (1996) The effect of inherited hydrocephalus and shunt treatment on cortical pyramidal cell dendrites in the infant H-Tx rat. Exp Neurol 141:269–279.

Hickman SE, Kingery ND, Ohsumi TK, Borowsky ML, Wang LC, Means TK, El Khoury J (2013) The microglial sensome revealed by direct RNA sequencing. Nat Neurosci 16:1896–1905.

Innocenti GM, Price DJ (2005) Exuberance in the development of cortical networks. Nat Rev Neurosci 6:955–965.

Jones HC, Bucknall RM, Harris NG (1991) The cerebral cortex in congenital hydrocephalus in the H-Tx rat: a quantitative light microscopy study. Acta Neuropathol 82:217–224.

Jones HC, Rivera KM, Harris NG (1995) Learning deficits in congenitally hydrocephalic rats and prevention by early shunt treatment. Childs Nerv Syst 11:655–660.

Jordão MJC, Sankowski R, Brendecke SM, Sagar, Locatelli G, Tai YH, Tay TL, Schramm E, Armbruster S, Hagemeyer N, Groß O, Mai D, Çiçek Ö, Falk T, Kerschensteiner M, Grün D, Prinz M (2019) Single-cell profiling identifies myeloid cell subsets with distinct fates during neuroinflammation. Science 363:eaat7554.

Kahle KT, Kulkarni AV, Limbrick DD, Warf BC (2016) Hydrocephalus in children. Lancet 387:788–799.

Karimy JK, Zhang J, Kurland DB, Theriault BC, Duran D, Stokum JA, Furey CG, Zhou X, Mansuri MS, Montejo J, Vera A, DiLuna ML, Delpire E, Alper SL, Gunel M, Gerzanich V, Medzhitov R, Simard JM, Kahle KT (2017) Inflammation-dependent cerebrospinal fluid hypersecretion by the choroid plexus epithelium in posthemorrhagic hydrocephalus. Nat Med 23:997–1003.

Karimy JK, Reeves BC, Damisah E, Duy PQ, Antwi P, David W, Wang K, Schiff SJ, Limbrick DD, Alper SL, Warf BC, Nedergaard M, Simard JM, Kahle KT (2020a) Inflammation in acquired hydrocephalus: pathogenic mechanisms and therapeutic targets. Nat Rev Neurol 16:285–296.

Karimy JK, Reeves BC, Kahle KT (2020b) Targeting TLR4-dependent inflammation in post-hemorrhagic brain injury. Expert Opin Ther Targets 24:525–533.

Kast RJ, Levitt P (2019) Precision in the development of neocortical architecture: from progenitors to cortical networks. Prog Neurobiol 175:77–95.

Kaur C, Dheen ST, Ling EA (2007) From blood to brain: amoeboid microglial cell, a nascent macrophage and its functions in developing brain. Acta Pharmacol Sin 28:1087–1096.

Khan OH, Enno TL, Del Bigio MR (2006) Brain damage in neonatal rats following kaolin induction of hydrocephalus. Exp Neurol 200:311–320.

Kiesler J, Ricer R (2003) The abnormal fontanel. Am Fam Physician 67:2547–2552.

Killer M, Arthur A, Al-Schameri AR, Barr J, Elbert D, Ladurner G, Shum J, Cruise G (2010) Cytokine and growth factor concentration in cerebrospinal fluid from patients with hydrocephalus following endovascular embolization of unruptured aneurysms in comparison with other types of hydrocephalus. Neurochem Res 35:1652–1658.

Klebe D, McBride D, Krafft PR, Flores JJ, Tang J, Zhang JH (2020) Posthemorrhagic hydrocephalus development after germinal matrix hemorrhage: established mechanisms and proposed pathways. J Neurosci Res 98:105–120.

Kostović I, Jovanov-Milošević N (2006) The development of cerebral connections during the first 20-45 weeks' gestation. Semin Fetal Neonatal Med 11:415–422.

Kriebel RM, Shah AB, McAllister JP (1993) The microstructure of cortical neuropil before and after decompression in experimental infantile hydrocephalus. Exp Neurol 119:89–98.

Kroon T, van Hugte E, van Linge L, Mansvelder HD, Meredith RM (2019) Early postnatal development of pyramidal neurons across layers of the mouse medial prefrontal cortex. Sci Rep 9:5037.

Kurt G, Cemil B, Borcek AO, Borcek P, Akyurek N, Sepici A, Ceviker N (2010) Infliximab administration reduces neuronal apoptosis on the optic pathways in a rabbit hydrocephalus model: a preliminary report. Br J Neurosurg 24:290–294.

Kwan KY, Šestan N, Anton ES (2012) Transcriptional co-regulation of neuronal migration and laminar identity in the neocortex. Development 139:1535–1546.

Lalioti ME, Kaplani K, Lokka G, Georgomanolis T, Kyrousi C, Dong W, Dunbar A, Parlapani E, Damianidou E, Spassky N, Kahle KT, Papantonis A, Lygerou Z, Taraviras S (2019) GemC1 is a critical switch for neural stem cell generation in the postnatal brain. Glia 67:2360–2373.

Larsen DLD, Callaway EM (2006) Development of layer-specific axonal arborizations in mouse primary somatosensory cortex. J Comp Neurol 494:398–414.

Lattke M, Magnutzki A, Walther P, Wirth T, Baumann B (2012) Nuclear factor κB activation impairs ependymal ciliogenesis and links neuroinflammation to hydrocephalus formation. J Neurosci 32:11511–11523.

Lenz KM, Nelson LH (2018) Microglia and beyond: innate immune cells as regulators of brain development and behavioral function. Front Immunol 9:698.

Lim L, Mi D, Llorca A, Marín O (2018) Development and functional diversification of cortical interneurons. Neuron 100:294–313.

Lindtner S, Catta-Preta R, Tian H, Su-Feher L, Price JD, Dickel DE, Greiner V, Silberberg SN, McKinsey GL, McManus MT, Pennacchio LA, Visel A, Nord AS, Rubenstein JLR (2019) Genomic resolution of DLX-orchestrated transcriptional circuits driving development of forebrain GABAergic neurons. Cell Rep 28:2048–2063.

Liu C, Li Y, Yu J, Feng L, Hou S, Liu Y, Guo M, Xie Y, Meng J, Zhang H, Xiao B, Ma C (2013) Targeting the shift from M1 to M2 macrophages in

experimental autoimmune encephalomyelitis mice treated with fasudil. PLoS One 8:e54841.

Macdonald RL, Kelly KM (1995) Antiepileptic drug mechanisms of action. Epilepsia 36:S2–S12.

Markram H, Toledo-Rodriguez M, Wang Y, Gupta A, Silberberg G, Wu C (2004) Interneurons of the neocortical inhibitory system. Nat Rev Neurosci 5:793–807.

McAllister JP, Miller JM (2010) Minocycline inhibits glial proliferation in the H-Tx rat model of congenital hydrocephalus. Cerebrospinal Fluid Res 7:7.

McAllister JP, Maugans TA, Shah MV, Truex RC (1985) Neuronal effects of experimentally induced hydrocephalus in newborn rats. J Neurosurg 63:776–783.

McAllister JP, Mangano FT, Jones HC, Kriebel RM (1998) The microglial response in experimental infantile hydrocephalus. Eur J Pediatr Surg 8:62.

Miller JM, McAllister JP (2007) Reduction of astrogliosis and microgliosis by cerebrospinal fluid shunting in experimental hydrocephalus. Cerebrospinal Fluid Res 4:5.

Mora E, Guglielmotti A, Biondi G, Sassone-Corsi P (2012) Bindarit: an anti-inflammatory small molecule that modulates the NFκB pathway. Cell Cycle 11:159–169.

Mosser CA, Baptista S, Arnoux I, Audinat E (2017) Microglia in CNS development: shaping the brain for the future. Prog Neurobiol 149–150:1–20.

Moyon S, Dubessy AL, Aigrot MS, Trotter M, Huang JK, Dauphinot L, Potier MC, Kerninon C, Parsadaniantz SM, Franklin RRJM, Lubetzki C (2015) Demyelination causes adult CNS progenitors too revert to an immature state and express immune cues that support their migration. J Neurosci 35:4–20.

Mukhtar T, Taylor V (2018) Untangling cortical complexity during development. J Exp Neurosci 12:117906951875933.

Nahmani M, Erisir A (2005) VGluT2 immunochemistry identifies thalamocortical terminals in layer 4 of adult and developing visual cortex. J Comp Neurol 484:458–473.

Namikawa T, Kikkawa S, Inokuchi G, Terashima T (2015) Postnatal development of the corticospinal tract in the Reeler mouse. Kobe J Med Sci 61: E71–E81.

Oddi S, Scipioni L, Totaro A, Angelucci C, Dufrusine B, Sabatucci A, Tortolani D, Coletta I, Alisi MA, Polenzani L, Assfalg M, Caltagirone C, Dainese E, Maccarrone M (2019) The anti-inflammatory agent bindarit acts as a modulator of fatty acid-binding protein 4 in human monocytic cells. Sci Rep 9:15155.

Park HJ, Kong JH, Kang YS, Park WM, Jeong SA, Park SM, Lim JK, Jeon CJ (2002) The distribution and morphology of calbindin D28K- and calretinin- immunoreactive neurons in the visual cortex of mouse. Mol Cells 14:143–149.

Pattisapu JV (2001) Etiology and clinical course of hydrocephalus. Neurosurg Clin N Am 12:651–659.

Paulsen AH, Lundar T, Lindegaard KF (2015) Pediatric hydrocephalus: 40-year outcomes in 128 hydrocephalic patients treated with shunts during childhood. Assessment of surgical outcome, work participation, and health-related quality of life. J Neurosurg Pediatr 16:633–641.

Platel JC, Bordey A (2016) The multifaceted subventricular zone astrocyte: from a metabolic and pro-neurogenic role to acting as a neural stem cell. Neuroscience 323:20–28.

Platten M, Kretz A, Naumann U, Aulwurm S, Egashira K, Isenmann S, Weller M (2003) Monocyte chemoattractant protein-1 increases microglial infiltration and aggressiveness of gliomas. Ann Neurol 54:388–392.

Raghanti MA, Spocter MA, Butti C, Hof PR, Sherwood CC (2010) A comparative perspective on minicolumns and inhibitory GABAergic interneurons in the neocortex. Front Neuroanat 4:3.

Raghu H, Lepus CM, Wang Q, Wong HH, Lingampalli N, Oliviero F, Punzi L, Giori NJ, Goodman SB, Chu CR, Sokolove JB, Robinson WH (2017) CCL2/CCR2, but not CCL5/CCR5, mediates monocyte recruitment, inflammation, and cartilage destruction in osteoarthritis. Ann Rheum Dis 76:914–922.

Rekate H (1999) Treatment of hydrocephalus. In: Principles and practice of pediatric neurosurgery (Albright AL, ed), pp 47–74. New York: Thieme.

Robinson S (2012) Neonatal posthemorrhagic hydrocephalus from prematurity: pathophysiology and current treatment concepts. J Neurosurg Pediatr 9:242–258.

Robson EA, Dixon L, Causon L, Dawes W, Benenati M, Fassad M, Hirst RA, Kenia P, Moya EF, Patel M, Peckham D, Rutman A, Mitchison HM, Mankad K, O'Callaghan C (2020) Hydrocephalus and diffuse choroid plexus hyperplasia in primary ciliary dyskinesia-related MCIDAS mutation. Neurol Genet 6:e482.

Rosin JM, Vora SR, Kurrasch DM (2018) Depletion of embryonic microglia using the CSF1R inhibitor PLX5622 has adverse sex-specific effects on mice, including accelerated weight gain, hyperactivity and anxiolytic-like behaviour. Brain Behav Immun 73:682–697.

Ross EJ, Graham DL, Money KM, Stanwood GD (2015) Developmental consequences of fetal exposure to drugs: what we know and what we still must learn. Neuropsychopharmacology 40:61–87.

Ryu Y, Ogata T, Nagao M, Kitamura T, Morioka K, Ichihara Y, Doi T, Sawada Y, Akai M, Nishimura R, Fujita N N (2017) The swimming test is effective for evaluating spasticity after contusive spinal cord injury. PLoS One 12:e0171937.

Ryu Y, Ogata T, Nagao M, Sawada Y, Nishimura R, Fujita N (2021) Early escitalopram administration as a preemptive treatment strategy against spasticity after contusive spinal cord injury in rats. Sci Rep 11:7120.

Rulli NE, Guglielmotti A, Mangano G, Rolph MS, Apicella C, Zaid A, Suhrbier A, Mahalingam S (2009) Amelioration of alphavirus-induced arthritis and myositis in a mouse model by treatment with bindarit, an inhibitor of monocyte chemotactic proteins. Arthritis Rheum 60:2513–2523.

Savman K, Blennow M, Hagberg H, Tarkowski E, Thoresen M, Whitelaw A (2002) Cytokine response in cerebrospinal fluid from preterm infants with posthaemorrhagic ventricular dilatation. Acta Paediatr 91:1357–1363.

Schmitz T, Heep A, Groenendaal F, Hüseman D, Kie S, Bartmann P, Obladen M, Felderhoff-Müser U (2007) Interleukin-1beta, interleukin-18, and interferon-gamma expression in the cerebrospinal fluid of premature infants with posthemorrhagic hydrocephalus–markers of white matter damage? Pediatr Res 61:722–726.

Schafer DP, Stevens B (2015) Microglia function in central nervous system development and plasticity. Cold Spring Harb Perspect Biol 7:a020545.

Shen Z, Kuang S, Zhang M, Huang X, Chen J, Guan M, Qin W, Xu HHK, Lin Z (2021) Inhibition of CCL2 by bindarit alleviates diabetes-associated periodontitis by suppressing inflammatory monocyte infiltration and altering macrophage properties. Cell Mol Immunol 18:2224–2235.

Shi Q, Colodner KJ, Matousek SB, Merry K, Hong S, Kenison JE, Frost JL, Le KX, Li S, Dodart JC, Caldarone BJ, Stevens B, Lemere CA (2015) Complement C3-deficient mice fail to display age-related hippocampal decline. J Neurosci 35:13029–13042.

Shirane R, Sato S, Sato K, Kameyama M, Ogawa A, Yoshimoto T, Hatazawa J, Ito M (1992) Cerebral blood flow and oxygen metabolism in infants with hydrocephalus. Childs Nerv Syst 8:118–123.

Smolders SMT, Kessels S, Vangansewinkel T, Rigo JM, Legendre P, Brône B (2019) Microglia: brain cells on the move. Prog Neurobiol 178:101612.

Squarzoni P, Oller G, Hoeffel G, Pont-Lezica L, Rostaing P, Low D, Bessis A, Ginhoux F, Garel S (2014) Microglia modulate wiring of the embryonic forebrain. Cell Rep 8:1271–1279.

Stottmann RW, Moran JL, Turbe-Doan A, Driver E, Kelley M, Beier DR (2011) Focusing forward genetics: a tripartite ENU screen for neurodevelopmental mutations in the mouse. Genetics 188:615–624.

Subramanian A, Tamayo P, Mootha VK, Mukherjee S, Ebert BL, Gillette MA, Paulovich A, Pomeroy SL, Golub TR, Lander ES, Mesirov JP (2005) Gene set enrichment analysis: a knowledge-based approach for interpreting genome-wide expression profiles. Proc Natl Acad Sci USA 102:15545–15550.

Suda K, Sato K, Takeda N, Miyazawa T, Arai H (1994) Early ventriculoperitoneal shunt - effects on learning ability and synaptogenesis of the brain in congenitally hydrocephalic HTX rats. Childs Nerv Syst 10:19–23.

Tanaka Y, Matsuwaki T, Yamanouchi K, Nishihara M (2013) Increased lysosomal biogenesis in activated microglia and exacerbated neuronal damage after traumatic brain injury in progranulin-deficient mice. Neuroscience 250:8–19.

Treiman DM (2001) GABAergic mechanisms in epilepsy. Epilepsia 42:8–12.

Tsai PT, Green-Colozzi E, Goto J, Anderl S, Kwiatkowski D, Sahin M (2013) Prenatal rapamycin results in early and late behavioral abnormalities in wildtype C57Bl/6 mice. Behav Genet 43:51–59.

Ulfig N, Bohl J, Neudörfer F, Rezaie P (2004) Brain macrophages and microglia in human fetal hydrocephalus. Brain Dev 26:307–315.

Van Vliet EA, Forte G, Holtman L, den Burger JCG, Sinjewel A, de Vries HE, Aronica E, Gorter JA (2012) Inhibition of mammalian target of rapamycin reduces epileptogenesis and blood-brain barrier leakage but not microglia activation. Epilepsia 53:1254–1263.

Vinchon M, Rekate H, Kulkarni AV (2012) Pediatric hydrocephalus outcomes: a review. Fluids Barriers CNS 9:18.

Virtanen MA, Lacoh CM, Fiumelli H, Kosel M, Tyagarajan S, De Roo M, Vutskits L (2018) Development of inhibitory synaptic inputs on layer 2/3 pyramidal neurons in the rat medial prefrontal corotex. Brain Struct Funct 223:1999–2012.

Wallmeier J, Frank D, Shoemark A, Nöthe-Menchen T, Cindric S, Olbrich H, Loges NT, Aprea I, Dougherty GW, Pennekamp P, Kaiser T, Mitchison HM, Hogg C, Carr SB, Zariwala MA, Ferkol T, Leigh MW, Davis SD, Atkinson J, Dutcher SK, et al. (2019) De novo mutations in FOXJ1 result in a motile ciliopathy with hydrocephalus and randomization of left/right body asymmetry. Am J Hum Genet 105:1030–1039.

Wang Y, Dye CA, Sohal V, Long JE, Estrada RC, Roztocil T, Lufkin T, Deisseroth K, Baraban SC, Rubenstein JLR (2010) Dlx5 and Dlx6 regulate the development of parvalbumin-expressing cortical interneurons. J Neurosci 30:5334–5345.

Wieters F, Lucas CW, Gruhn M, Büschges A, Fink GR, Aswendt M (2021) Introduction to spasticity and related mouse models. Exp Neurol 335:113491.

Wu KY, Tang FL, Lee D, Zhao Y, Song H, Zhu XJ, Mei L, Xiong WC (2020) Ependymal Vps35 promotes ependymal cell differentiation and survival, suppresses microglial activation, and prevents neonatal hydrocephalus. J Neurosci 40:3862–3879.

Wys-Coray T, Feng L, Masliah E, Ruppe MD, Lee HS, Toggas SM, ROckenstein EM, Mucke L (1995) Increased central nervous system production of extracellular matrix components and development of hydrocephalus in transgenic mice overexpressing transforming growth factor-beta 1. Am J Pathol 147:53–67.

Zhang J, Shi X, Chen Z, Geng J, Wang Y, Feng H, Zhu G, Chen Q (2018a) Edaravone reduces iron-mediated hydrocephalus and behavioral disorder in rat by activating the Nrf2/HO-1 pathway. J Stroke Cerebrovasc Dis 27:3511–3520.

Zhang K, Wang H, Xu M, Frank JA, Luo J (2018b) Role of MCP-1 and CCR2 in ethanol-induced neuroinflammation and neurodegeneration in the developing brain. J Neuroinflammation 15:197.

Zhang LY, Pan J, Mamtilahun M, Zhu Y, Wang L, Venkatesh A, Shi R, Tu X, Jin K, Wang Y, Zhang Z, Yang GY (2020) Microglia exacerbate white matter injury via complement C3/C3aR pathway after hypoperfusion. Theranosotics 10:74–90.

Zhong S, Zhang S, Fan X, Wu Q, Yan L, Dong J, Zhang H, Li L, Sun L, Pan N, Xu X, Tang F, Zhang J, Qiao J, Wang X (2018) A single-cell RNA-seq survey of the developmental landscape of the human prefrontal cortex. Nature 555:524–528.

Zhou T, Huang Z, Sun X, Zhu X, Zhou L, Li M, Cheng B, Liu X, He C (2017) Microglia polarization with M1/M2 phenotype changes in rd1 mouse model of retinal degeneration. Front Neuroanat 11:77.